

Award Number: W81XWH-10-1-0743

TITLE: A Novel Multivoxel-Based Quantitation of Metabolites and Lipids Noninvasively Combined with Diffusion-Weighted Imaging in Breast Cancer

PRINCIPAL INVESTIGATOR: Michael Albert Thomas Ph.D.

CONTRACTING ORGANIZATION: University of California, Los Angeles  
Los Angeles, CA 90024-1406

REPORT DATE: September 2012

TYPE OF REPORT: Annual

PREPARED FOR: U.S. Army Medical Research and Materiel Command  
Fort Detrick, Maryland 21702-5012

DISTRIBUTION STATEMENT: Approved for Public Release;  
Distribution Unlimited

The views, opinions and/or findings contained in this report are those of the author(s) and should not be construed as an official Department of the Army position, policy or decision unless so designated by other documentation.

# REPORT DOCUMENTATION PAGE

*Form Approved*  
*OMB No. 0704-0188*

Public reporting burden for this collection of information is estimated to average 1 hour per response, including the time for reviewing instructions, searching existing data sources, gathering and maintaining the data needed, and completing and reviewing this collection of information. Send comments regarding this burden estimate or any other aspect of this collection of information, including suggestions for reducing this burden to Department of Defense, Washington Headquarters Services, Directorate for Information Operations and Reports (0704-0188), 1215 Jefferson Davis Highway, Suite 1204, Arlington, VA 22202-4302. Respondents should be aware that notwithstanding any other provision of law, no person shall be subject to any penalty for failing to comply with a collection of information if it does not display a currently valid OMB control number. **PLEASE DO NOT RETURN YOUR FORM TO THE ABOVE ADDRESS.**

<b>1. REPORT DATE</b> September 2012		<b>2. REPORT TYPE</b> Annual		<b>3. DATES COVERED</b> 1 September 2011- 31 August 2012		
<b>4. TITLE AND SUBTITLE</b> A Novel Multivoxel-Based Quantitation of Metabolites and Lipids Noninvasively Combined with Diffusion-Weighted Imaging in Breast Cancer				<b>5a. CONTRACT NUMBER</b>		
				<b>5b. GRANT NUMBER</b> W81XWH-10-1-0743		
				<b>5c. PROGRAM ELEMENT NUMBER</b>		
<b>6. AUTHOR(S)</b> Michael Albert Thomas Ph.D.  <b>E-Mail:</b>				<b>5d. PROJECT NUMBER</b>		
				<b>5e. TASK NUMBER</b>		
				<b>5f. WORK UNIT NUMBER</b>		
<b>7. PERFORMING ORGANIZATION NAME(S) AND ADDRESS(ES)</b> University of California, Los Angeles Los Angeles, CA 90095				<b>8. PERFORMING ORGANIZATION REPORT NUMBER</b>		
<b>9. SPONSORING / MONITORING AGENCY NAME(S) AND ADDRESS(ES)</b> U.S. Army Medical Research and Materiel Command Fort Detrick, Maryland 21702-5012				<b>10. SPONSOR/MONITOR'S ACRONYM(S)</b>		
				<b>11. SPONSOR/MONITOR'S REPORT NUMBER(S)</b>		
<b>12. DISTRIBUTION / AVAILABILITY STATEMENT</b> Approved for Public Release; Distribution Unlimited						
<b>13. SUPPLEMENTARY NOTES</b>						
<b>14. ABSTRACT-</b> Purpose: i) To extend the single-voxel based 2D MRS version of L-COSY to multi-voxel based analogue on a 3T MRI/MRS scanner using the echo-planar imaging (EPI) based spatial encoding for determining metabolic distributions over many voxels, ii) To implement a Matlab-based post-processing algorithm in order to process the 2D COSY data recorded in breast cancer, iii) To record DWI and to calculate ADC maps in breast cancer patients and healthy controls, and iv) To correlate the changes in metabolite and lipid levels with ADC changes in breast cancer patients and healthy women. Scope: Improving the specificity of malignant and benign tumors will be a major outcome. Improved imaging techniques will enable unambiguous measurement of metabolites and the lipids in situ, which could potentially complement the existing diagnostic modalities commonly used in breast carcinoma. Major Findings: The MR protocol including 4D EP-COSI and DWI-MRI was successfully evaluated in six healthy women, 3 benign and 2 malignant breast cancer patients on a 3T MRI scanner. Report of the Progress: Multi-slice DWI-MRI and 4D EP-COSI was tested in 2 malignant and 3 benign breast cancer patients and 6 healthy women. The ADC maps using DWI and lipid/water images using EP-COSI have been derived. DWI images showed reduced ADC values in affected mass and the EP-COSI data showing lipid and metabolite changes in breast cancer						
<b>15. SUBJECT TERMS-</b> MAGNETIC RESONANCE IMAGING, MAGNETIC RESONANCE SPECTROSCOPY, Echo Planar Correlated Spectroscopic Imaging, DIFFUSION WEIGHTED IMAGING, APPARENT DIFFUSION COEFFICIENT, CHOLINE, LIPIDS, WATER, SATURATED AND UNSATURATED LIPIDS						
<b>16. SECURITY CLASSIFICATION OF:</b>				<b>17. LIMITATION OF ABSTRACT</b>	<b>18. NUMBER OF PAGES</b>	<b>19a. NAME OF RESPONSIBLE PERSON</b> USAMRMC
<b>a. REPORT</b> U	<b>b. ABSTRACT</b> U	<b>c. THIS PAGE</b> U	<b>19b. TELEPHONE NUMBER</b> (include area code)			

## Table of Contents

	<u>Page</u>
<b>Introduction.....</b>	<b>4</b>
<b>Body.....</b>	<b>4</b>
<b>Key Research Accomplishments.....</b>	<b>10</b>
<b>Reportable Outcomes.....</b>	<b>10</b>
<b>Conclusion.....</b>	<b>11</b>
<b>References.....</b>	<b>11</b>
<b>Appendices.....</b>	<b>13</b>

## **Introduction:**

A leading cause of cancer deaths among women worldwide is due to breast cancer and new therapies and optimal treatments are continuously being conceived and explored to better control or even cure this disease. (1). Diagnosis and therapeutic management of the breast tumor remain significant medical challenges, hence early detection, diagnosis, and timely treatments are essential to successful health care (2). Magnetic resonance imaging and spectroscopy (MRI/MRS) have gained significant importance during the last fifteen years for the diagnosis and monitoring of breast cancer therapy. The sensitivity of MRI/MRS for anatomical delineation is very high and the consensus is that MRI is more sensitive in detection than x-ray mammography. Advantages of MRS include delivery of biochemical information about tumor metabolism, which can potentially assist in the staging of cancers and monitoring responses to treatment. High sensitivity is a major advantage of contrast enhanced MRI, but its diagnostic relevance in the future will largely depend on improvements in specificity. Current approaches in the application of MRI to breast tumors aim to improve specificity and sensitivity (4-17). Increased specificity is necessary to reduce the number of biopsies performed to confirm false positive findings. Diffusion-weighted imaging (DWI) is another MR based technique that probes the microstructure of tissues and is sensitive to the degree to which motion of water molecules is restricted in relation to how packed together cells are (17, 18). It has been reported that high resolution DWI may add valuable functional information to conventional MR protocols with short measurement times for the diagnosis of breast cancer and improve the specificity of MR imaging (19-21). However, new technological developments are necessary to assess their role in breast diagnosis. A method capable of identifying biochemical characteristics non-invasively in the tumor lesions that can be used in conjunction with MRI is proton ( $^1\text{H}$ ) MR Spectroscopy (MRS). Researchers have shown that  $^1\text{H}$  MRS can be used to characterize breast cancers with improved diagnostic accuracy (22-26). Unfortunately, multi-voxel based novel MR spectroscopic imaging (MRSI) techniques using the speed advantage offered by echo-planar imaging (EPI) and improved spectral resolution offered by two-dimensional (2D) MR spectroscopy (MRS) have not been fully explored in breast cancer studies so far. Hence, a major task of this project is to combine echo-planar correlated spectroscopic imaging (EP-COSI) with DWI approach for improving the overall specificity of breast cancer detection.

## **Body:**

*i) **Proposed Task 1:** To further optimize the multi-voxel based extension of the correlated spectroscopy (COSY) sequence, in which two spectral encodings will be combined with two spatial encodings. This four-dimensional (4D) data acquisition scheme will be accomplished utilizing the echo-planar imaging (EPI) approach that is commonly used for spatial encoding in MRI including DWI. (Months 1-6).*

This task was completed already (September 2010-May 2011) as reported last year.

*ii) **Proposed Task 2:** To evaluate the EP-COSI data using a breast phantom containing two concentric spheres, the inner one containing several metabolites which have been reported in breast tissues surrounded by the outer phantom containing corn oil to mimic*

fatty tissues known to be in breast tissues, and to optimize the echo speed-factor and other acquisition parameters using the phantom (**Months 1-6**).

This task was completed already (September 2010-August 2011) as reported again last year.

**iii) Proposed Task 3:** To develop, evaluate and optimize the prior-knowledge basis set spectra using the GAMMA-simulation and breast phantom solutions as prior knowledge for the multi-voxel based COSY spectra recorded using the 3T MRI scanner (**Months 3-9**).

Using the GAMMA library (27), a prior-knowledge basis-set containing metabolites and lipids was prepared (April 2010-August 2011) as reported last year.

**iv) Proposed Task 4:** To record the EP-COSI spectra in the fatty, glandular and ductal areas of healthy breasts. Twenty healthy female volunteers (25-70 years old) with no previous history of breast cancer will be investigated. (**Months 6-24**).

Five healthy women (age=36-59 years) were investigated using the DWI and EP-COSI MRI protocol as reported earlier (March 2011-July 2011). Six more healthy women (age=26-46 years) without any prehistory of breast cancer have been studied during the 2<sup>nd</sup> year. The ADC image derived from the DWI data recorded in a 34 yo healthy woman is shown in Fig.1. Feasibility of recording 2D COSY spectra in multiple regions using the EP-COSI sequence is demonstrated in Fig.2. Multi-voxel metabolite spectra of the fat peak at 5.3ppm is shown in Fig.2B (28). 2D MR spectra were recorded in multiple regions including the fatty and glandular regions of the 34 yo healthy subject as shown in Fig.2C and D. C and D were extracted COSY spectra from the fatty and glandular regions

<sup>3</sup> with a volume of 1x1x2cm . These findings were reproduced in other 10 ten healthy women as shown in our earlier manuscript using a single voxel (SV) localized L-COSY sequence (29).

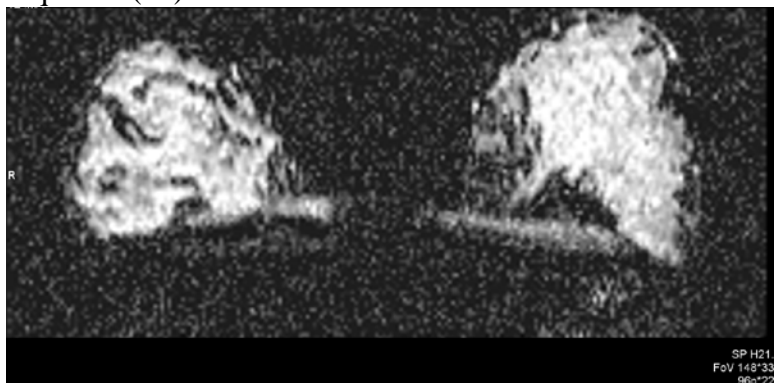


**Figure 1. A)** An axial ADC slice image recorded in a 34 yo healthy subject using the DWI sequence.

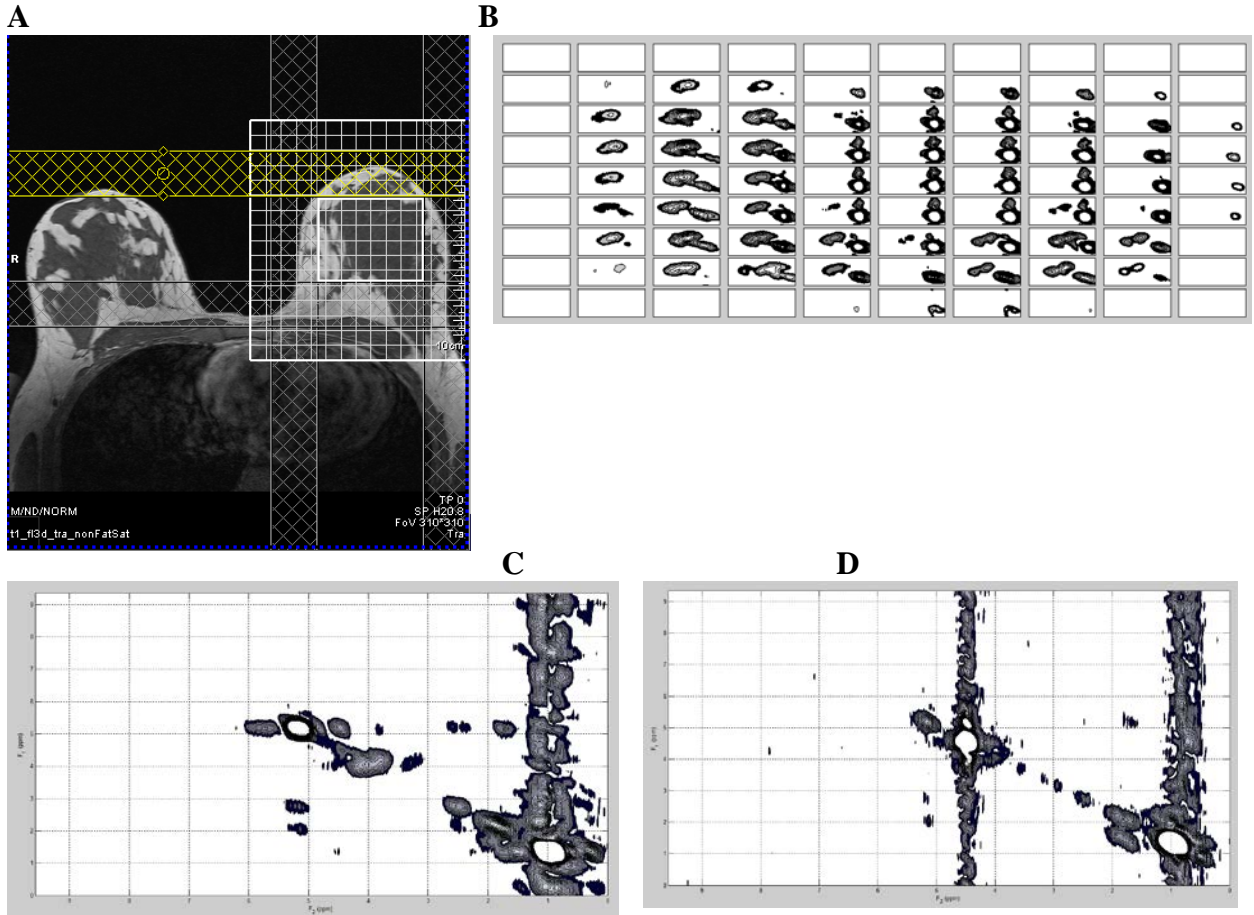


**Figure 2.** **A)** An axial MRI slice image recorded in the same healthy subject as above showing the EP-COSI localization; the small white box shows the regions of interest (ROI) localized the EP-COSI sequence and the large white box with 16x16 grids shows the spatial localization encoded by the EP-COSI sequence. **B)** Multi-voxel display of the EP-COSI data showing the olefinic diagonal peaks. **C)** and **D)** are 2ml 2D COSY spectra from the fatty and glandular regions extracted from the EP-COSI data.

**v) Proposed Task 5:** *To record the multi-voxel-based 2D spectra in patients with benign and malignant breast cancer. The breast metabolite and lipid concentrations calculated from the multi-voxel data using the ProFit algorithm will be compared with LC-Model processed 1D spectral based MRSI data. Twenty patients with biopsy-proven breast cancer (ductal carcinoma and invasive lobular cancer), twenty patients with benign breast tumor (fibroadenoma, proliferative fibrocystic change and papillomas) will be investigated (Months 6-24).*

Three women with benign (age=28-44 years) and 2 with malignant breast cancer (age=61 years) have been investigated using the 4D EP-COSI sequence on the 3T MRI scanner using a dedicated breast MRI coil. Shown in Fig. 3 are the following: **A)** An axial MRI slice image recorded in a 44yo benign cancer patient showing the EP-COSI localization. **B)** Multi-voxel EP-COSI spectra and **C)** a 2ml COSY spectrum recorded from the affected mass.

**A**

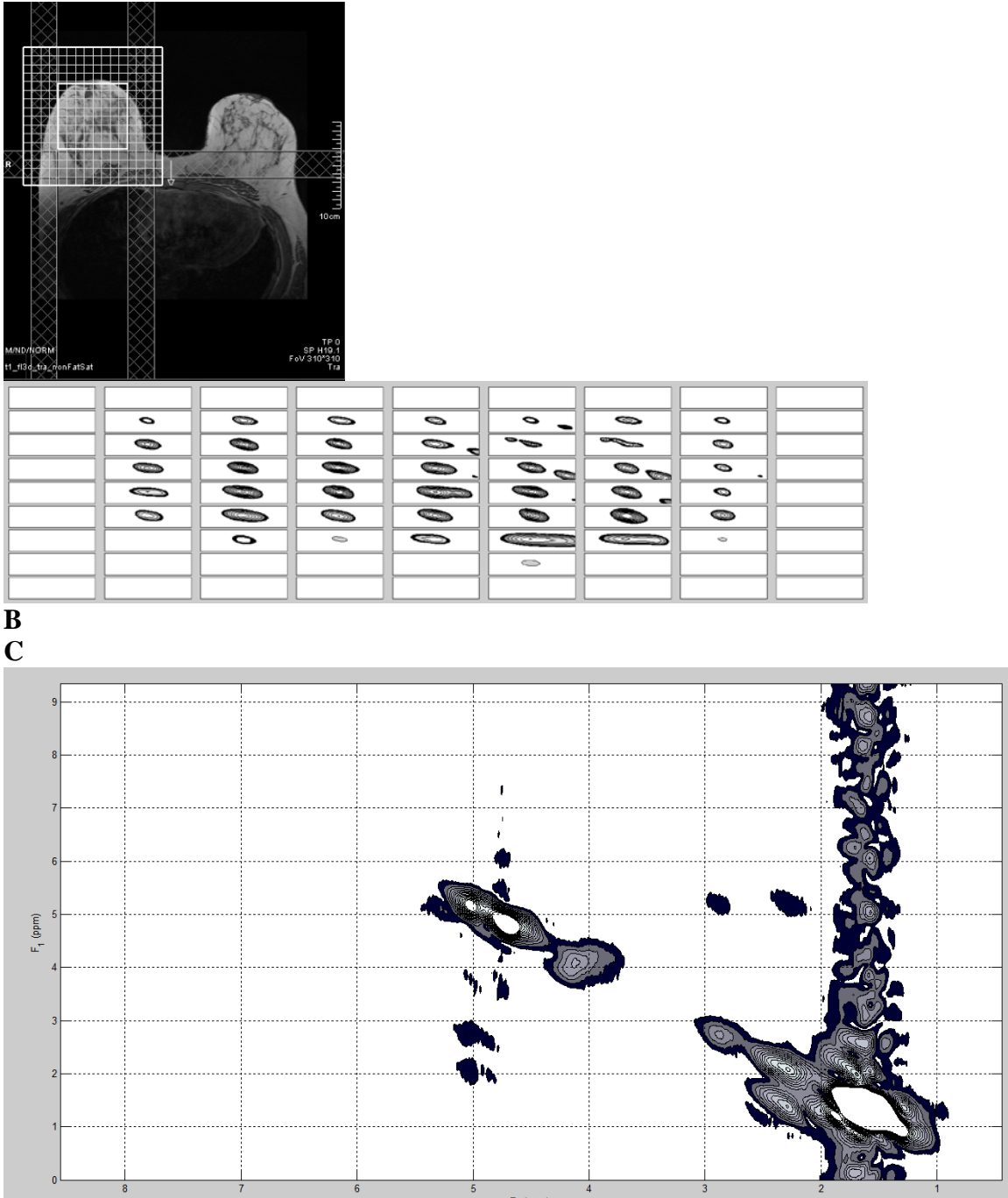
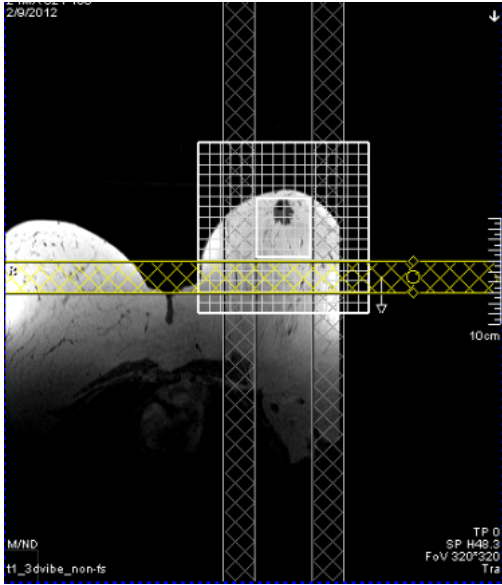
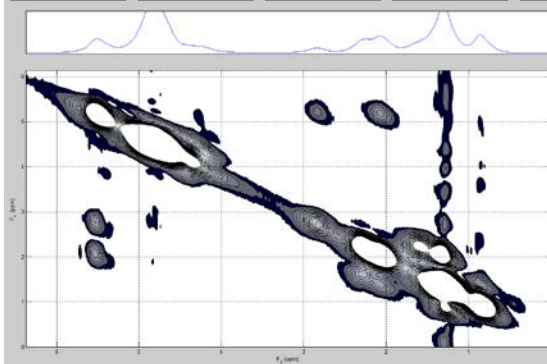
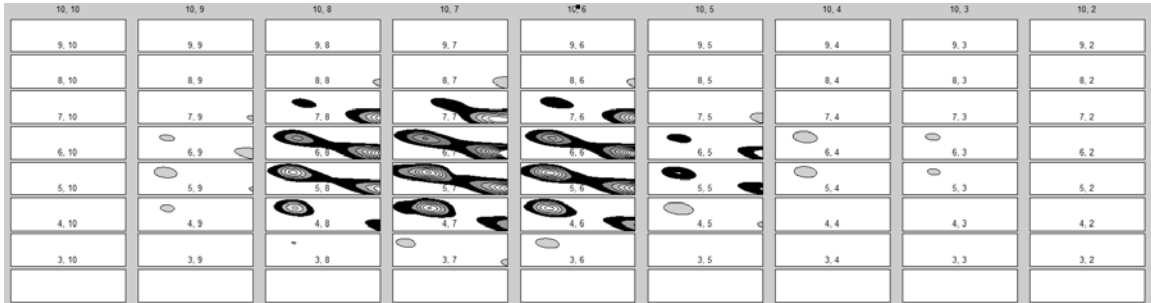


**Figure 3.** (A) An axial MRI slice image recorded in a 44 yo subject with benign breast cancer showing the EP-COSI localization; the small white box shows the regions of interest (ROI) localized the EP-COSI sequence and the large white box with 16x16 grids shows the spatial localization encoded by the EP-COSI sequence. (B) multi-voxel 2D COSY spectra covering fatty and glandular breast regions. (C) A 2ml benign lesion-indicating spectrum showing slightly increased water and slightly reduced lipids.

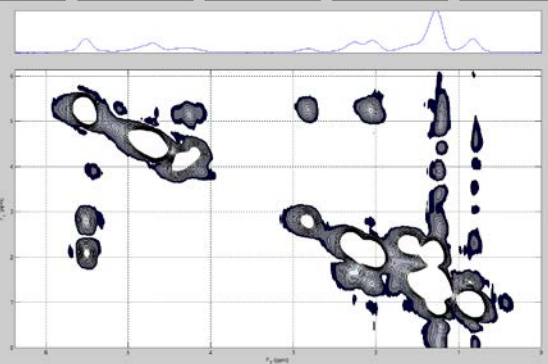
A



**B**



**C**



**D**

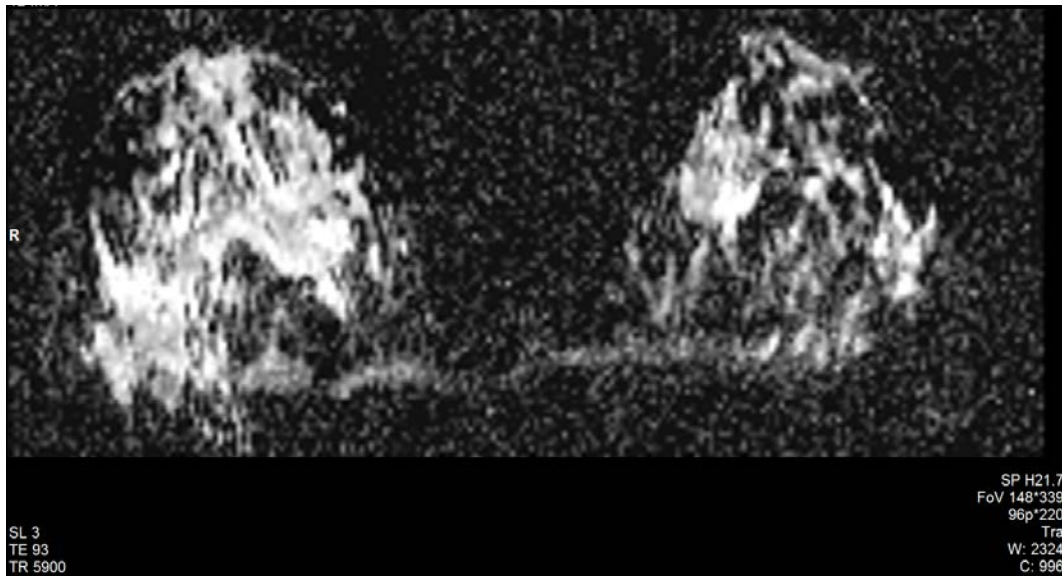
**Figure 4.** (A) An axial MRI slice image recorded in a 61 yo subject with malignant breast cancer (a hypo-intense mass) showing the EP-COSI localization; the small white box shows the regions of interest (ROI) localized the EP-COSI sequence and the large white box with 16x16 grids shows the spatial localization encoded by the EP-COSI sequence. (B) multi-voxel 2D COSY spectra covering fatty and glandular breast regions. (C) and (D) show 1ml spectra showing increased water and slightly reduced lipids.

Fig. 4 shows the following: A) An axial MRI slice image recorded in a 61yo malignant breast cancer patient showing the EP-COSI localization. B) Multi-voxel EP-COSI spectra; C) and D) show 2ml COSY spectra recorded from the affected mass and a

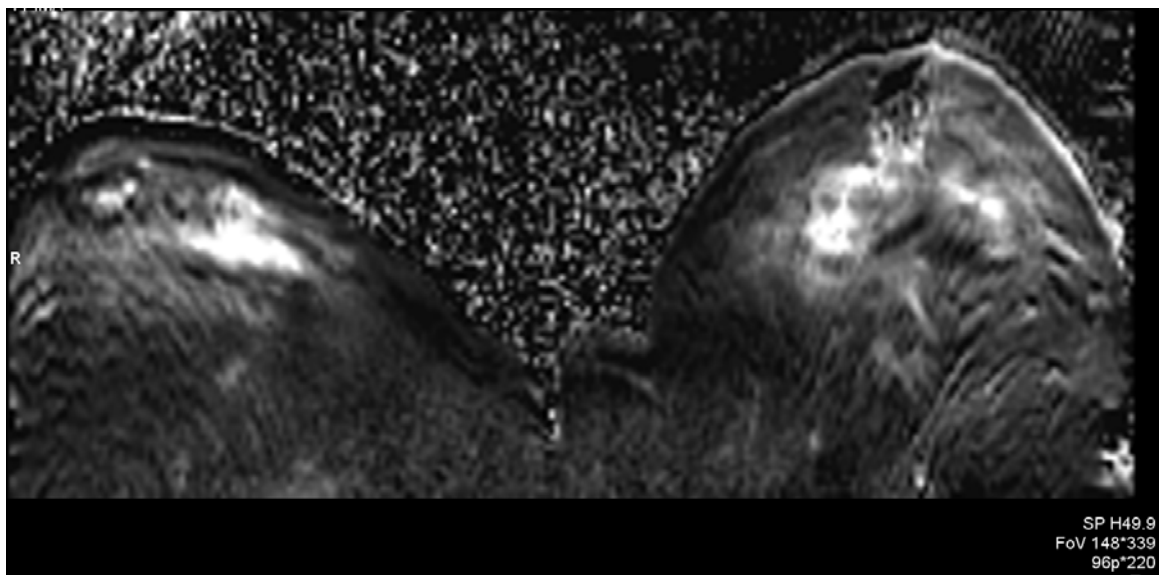
healthy region. These results are also in agreement with our earlier data on the SV-based L-COSY sequence (29-30).

**vi) Proposed Task 6:** *To record multi-slice DWI in twenty patients with biopsy-proven breast cancer, twenty patients with benign breast tumor and twenty healthy women and to calculate the ADC maps. (Months 6-24).*

**Figure 5.** An axial ADC slice image recorded in the 44 yo subject with a benign mass using the DWI sequence.



**Figure 6.** An axial ADC slice image recorded in the 61 yo subject with a malignant mass in the left breast using the DWI sequence.



The diffusion weighted imaging (DWI) has been recorded in three women with benign and 2 with malignant breast cancer 3T MRI scanner using a dedicated breast MRI coil.

**vii) Proposed Task 7:** *To correlate the EP-COSI findings with that of DWI in differentiating benign from malignant breast cancers, and to calculate specificity, sensitivity and accuracy of the MRSI and DWI data in differentiating benign from malignant tumors. (Months 6-24).*

This task will be completed during the next year.

### **Key Research Accomplishments**

- The 4D EP-COSI has been successfully evaluated in 11 healthy women, 3 benign and 2 malignant breast cancer patients so far using the UCLA Radiology Siemens 3T MRI scanner equipped with a dedicated breast phased-array assembly. As summarized in the last year report, this sequence is available now at UCLA only and is not supplied by any of MRI manufacturers.
- The DWI-MRI protocol was successfully evaluated in a total of 11 healthy women, 3 benign and 2 malignant breast cancer patients so far.
- We have demonstrated that the EP-COSI spectroscopic imaging sequence can be combined with a clinical breast DWI protocol with the total duration of less than an hour. The protocol is safe enough to be included in any MRI protocol to be evaluated in breast cancer for improving the overall specificity.
- We are currently testing retrospective Maximum Entropy and Compressed Sensing of the 4D EP-COSI data so that the acquisition can be accelerated in the near future to 5-10 minutes which will lead to less inconvenience to patients suffering from breast cancer.

### **Reportable Outcomes:**

**A. Peer-reviewed Publications:** Burns B, Wilson N and Thomas MA. Maximum Entropy Reconstruction of Non-Uniformly Under-Sampled Multi-dimensional MR Spectroscopic Imaging in vivo. Magn Reson Med 2012 (submitted).

**B. Presentations:** There were three conference presentations containing four abstracts.

- A Poster presentation at the International Society of Magnetic Resonance in Medicine (ISMRM) Conference 2012, Melbourne, Australia. *Maximum Entropy Reconstruction of Correlated Spectroscopy of Human Breast in vivo.* May 2012
- A Poster presentation at the International Society of Magnetic Resonance in Medicine (ISMRM) Conference 2012, Melbourne, Australia. *Maximum Entropy Based Reconstruction of Echo-Planar Correlated Spectroscopic Imaging of Human Breast in vivo.* May 2012
- A Poster presentation at the International Society of Biomedical Engineering (ISBI) Conference 2012, Barcelona, Spain. *Maximum Entropy Reconstruction of Echo-Planar Correlated Spectroscopic Imaging of Human Breast In Vivo.* May 2012.

- A Poster presentation at the 51<sup>st</sup> Experimental NMR Conference (ENC) , Orlando, Florida. Accelerated Multi-voxel two-dimensional in vivo spectroscopy using Compressed Sensing. April 2012

**C. Books:** None on Breast Cancer Research based.

**Conclusions:** The scanning protocol including EP-COSI and DWI-MRI has been evaluated in 11 healthy women, three benign and 2 malignant breast cancer so far. We will continue to recruit 10 malignant, 10 benign and 5 healthy women during the next year. Our inability in recruiting more breast cancer patients has been discussed with the UCLA mammo co-investigators, namely Dr. Naneltte DeBruhl and Dr. Lawrence Bassett. They have promised us to improve the patient recruitment in the 3<sup>rd</sup> year.

## **References**

1. Biersack B, Schobert R. Indole Compounds against Breast Cancer: Recent Developments. *Curr Drug Targets*. 2012 Nov 6. [Epub ahead of print].
2. Ries LAD, Eisner MP, Kosary CL, Hankey BF, Miller BA, Clegg L, Mariotto A, Feuer EJ, Edwards BK (eds). *SEER Cancer Statistics Review 1975-2002*. National Cancer Institute: Bethesda, MD. <http://seer.cancer.gov/csr/1975-2002/>, based on November 2004 SEER data submission, posted online 2005.
3. Sabel M and Aichinger H. Recent developments in breast imaging. *Phys Med Biol* 1996; 41 (3): 315-68.
4. Morris EA. Diagnostic Breast MR Imaging: Current Status and Future Directions. *Radiol Clin N America* 2007; 45: 863-880.
5. Lehman CD, Isaacs C, Schnall MD, Pisano ED, Ascher SM, Weatherall PT, Bluemke DA, Bowen DJ, Marcom PK, Armstrong DK, Domchek SM, Tomlinson G, Skates SJ, Gatsonis C. Cancer Yield of mammography, MR and US in high-risk women: Perspective multi-institution breast cancer screening study. *Radiology*. 2007; 244: 381-388.
6. Saslow D, Boetes C, Burke W, Harms S, Leach MO, Lehman CD, Morris E, Pisano E, Schnall M, Sener S, Smith RA, Warner E, Yaffe M, Andrews KS, Russell CA. American Cancer Society Guidelines for Breast Screening with MRI as an Adjunct to Mammography. *CA Cancer J Clin*. 2007; 57: 75-89.
7. Weinreb JC and Newstead G. MR imaging of the breast, *Radiology* 1995; 196(3): 593-610.
8. Harms SE and Flamig DP. MR imaging of the breast. *J Magnetic Resonance Imaging* 1993; 2:277-83.
9. Graham SJ, Bronskill MJ, et al. Quantitative correlation of breast tissue parameters using magnetic resonance and X-ray mammography. *British Journal Cancer* 1996; 73(2): 162-8.
10. Stelling CB. MR imaging of the breast for cancer evaluation. Current status and future directions. *Radiologic Clinics of North America* 1995; 33(6):1187-204.
11. Cohen EK, Leonhardt CM, Shumak RS, Soutar IC, Bukhanov K, Fishell EK, Plewes DB. Magnetic resonance imaging in potential post surgical recurrence of breast cancer: pitfalls and limitations. *Canadian Association of Radiologists Journal* 1996; 47(3):171-6.

12. Hickman PF, Moore NR and Shepstone BJ. The indeterminate breast mass: assessment-using contrast enhanced magnetic resonance imaging. *Brit J Radiology* 1994; 67(793):14-20.
13. Kerslake RW, Fox JN, Carleton PJ, Imrie MJ, Cook AM, Bowsley SJ, Horsman A. A dynamic contrast-enhanced and fat suppressed magnetic resonance imaging in suspected recurrent carcinoma of the breast: preliminary experience. *Brit J Radiology* 1994; 67(804): 1158-68.
14. Kvistad KA, Rydland J, Vainio J, Smethurst HB, Lundgren S, Fjøsne HE, Haraldseth O. Breast Lesions: evaluation with dynamic contrast-enhanced T1 weighted MR Imaging and with T2\* weighted first-pass perfusion MR imaging. *Radiology* 2000; 216: 545-553.
15. Furman-Haran E, Grobgeld D, Kelcz F, Degani H.. Critical role of spatial resolution in dynamic contrast-enhanced breast MRI. *J Magn Reson Imag* 2001; 13: 862-867.
16. Liu PF, Debatin JF, Caduff RF, Kacel G, Garzoli E, Krestin GP. Improved diagnostic accuracy in dynamic contrast-enhanced MRI of the breast by combined quantitative and qualitative analysis. *Brit J Rad* 1998; 71:501-509.
17. Le Bihan D, Breton E, Lallemand D, Renier P, Cabanis E, Laval-Jeantet M. MR imaging of intravoxel incoherent motions: application to diffusion and perfusion in neurologic disorders. *Radiology* 1986;161:401-407.
18. Bammer. Basic principles of diffusion-weighted imaging. *European journal of radiology*. 2003 Mar;45(3):169-84.
19. Belli P, Constantini M, Bufi E, Magistrelli A, La Torre G, Bonomo L. Diffusion weighted imaging in breast lesion evaluation. *Radiol Med* 2009.
20. Sharma U, Danishad KK, Seenu V, Jagannathan NR. Longitudinal study of the assessment by MRI and diffusion-weighted imaging of tumor response in patients with locally advanced breast cancer undergoing neoadjuvant chemotherapy. *NMR Biomed* 2009;22:104-113.
21. Bogner W, Gruber S, Pinker K, Grabner G, Stadlbauer A, Weber M, Moser E, Helbich TH, Trattnig S. Diffusion-weighted MR for Differentiation of Breast Lesions at 3.0 T: How Does Selection of Diffusion Protocols Affect Diagnosis? *Radiology* 2009;253:341-351
22. Gribbestad IS, Sitter B, Lundgren S, Krane J, Axelson D. Metabolite composition in breast tumors examined by proton nuclear magnetic resonance spectroscopy. *Anticancer Res* 1999; 19: 1737-1746.
23. Aboagye EO, Bhujwala ZM. Malignant transformation alters epithelial cells. *Cancer Res* 1999; 59(1): 80-84.
24. Mountford CE, Somorjai RL, Malycha P, Gluch L, Lean C, Russell P, Barraclough B, Gillett D, Himmelreich U, Dolenko B, Nikulin AE, Smith IC. Diagnosis and prognosis of breast cancer by magnetic resonance spectroscopy of fine-needle aspirates analyzed using a statistical classification strategy. *BR J Surg* 2001; 88: 1234-1240.
25. Stanwell P, Gluch L, Clark D, Tomanek B, Baker L, Giuffrè B, Lean C, Malycha P, Mountford C. Specificity of choline metabolites for in vivo diagnosis of breast cancer using <sup>1</sup>H MRS at 1.5T. *Eur. Radiology* 2005; 50: 1134-1143.
26. Roebuck JR, Cecil KM, Schnall MD, Lenkinski RE. Human breast lesions: characterization with proton MR spectroscopy. *Radiology* 1998; 209: 269-275.
27. Smith SA, Levante TO, Meier BH and Ernst RR. Computer Simulations in Magnetic Resonance. An object oriented programming approach. *J Magn Reson* 1994; A106: 75-105.
28. Lipnick S, Verma G, Ramadan S, Furuyama J and Thomas MA. Echo-Planar based Correlated Spectroscopic Imaging (EP-COSI): Implementation and Pilot Evaluation in Human Calf Muscle. *Magn Reson Med* 2010;64(4):947-956.
29. Thomas MA, Binesh N, Yue K and DeBruhl N. Volume-Localized Two-Dimensional Correlated Magnetic Resonance Spectroscopy of Human Breast Cancer. *J Magn Reson Imaging* 2001;14:181-

186.30. Lipnick S, Liu X, Sayre J, Bassett L, DeBruhl N and Thomas MA. Combined DCE-MRI and single-voxel 2D MRS for differentiation between benign and malignant breast lesions. *NMR Biomed* 2010; 23: 922–930.

**Appendix:**

- A)** A copy of our Poster presented at the at the International Society of Biomedical Engineering (ISBI) Conference 2012, Barcelona, Spain
- B)** A copy of our 1<sup>st</sup> Abstract entitled “*Maximum Entropy Reconstruction of Correlated Spectroscopy of Human Breast in vivo.*” at the International Society of Magnetic Resonance in Medicine (ISMRM) Conference 2012, Melbourne, Australia. May 2012.
- C)** A copy of our 2<sup>nd</sup> Abstract entitled “*Maximum Entropy Based Reconstruction of Echo-Planar Correlated Spectroscopic Imaging of Human Breast in vivo.*” at the International Society of Magnetic Resonance in Medicine (ISMRM) Conference 2012, Melbourne, Australia. May 2012.
- D)** A preprint of our manuscript currently under review: Burns B, Wilson N and Thomas MA. Maximum Entropy Reconstruction of Non-Uniformly Under-Sampled Multi-dimensional MR Spectroscopic Imaging in vivo. *Magn Reson Med* 2012 (submitted).

# MAXIMUM ENTROPY RECONSTRUCTION OF ECHO-PLANAR CORRELATED SPECTROSCOPIC IMAGING DATA OF HUMAN BREAST *IN VIVO*



Brian L. Burns and M. Albert Thomas

Departments of Biomedical Engineering and Radiological Sciences, David Geffen School of Medicine, University of California, Los Angeles, CA 90095

## Introduction

•4D Echo-Planar based Correlated Spectroscopic Imaging (EPCOSI) allows for the simultaneous acquisition of two spatial ( $k_y, k_x$ ) and two spectral ( $t_2, t_1$ ) dimensions *in vivo* in a single Magnetic Resonance (MR) experiment [1].

•The EPI readout accelerates the direct acquisition of the  $k_x$  and  $t_2$  dimensions but the  $k_y$  and  $t_1$  dimensions are incrementally acquired as indirect dimensions.

•Non-uniform under-sampling (NUS) the  $k_y$  and  $t_1$  dimensions to 25% and reconstructing the missing data with Maximum Entropy (MaxEnt) preserves the spectral and spatial resolution of the acquired data and reduces the scan time from 20 to 5 minutes in healthy human breast *in vivo*.

## Materials and Methods

•An EPCOSI scan of healthy breast with the following parameters:  $1x1x2cm^3$  voxel size, TR/TE=1.5s/30ms, 50  $t_1$  increments,  $16x16cm^2$  FOV was retrospectively NUS to 25% of the  $k_y$ - $t_1$  plane using the mask in Fig. 2.

•Missing data in the  $k_y$ - $t_1$  plane was reconstructed using MaxEnt [2,3]:

$$\text{maximize } S_{1/2}(f) \text{ s.t. } C(f) \leq \sigma \quad (1)$$

where  $f$  is the estimated fully-sampled spatially distributed spectra,  $C(f)$  is the time-domain fidelity constraint,  $\sigma$  is the noise standard deviation, and  $S_{1/2}(f)$  is the spin- $1/2$  entropy of the estimated spectra [4].

•The Cambridge MaxEnt algorithm uses a variant of the conjugate gradient method to solve (1) as shown in Fig. 3.

## Results and Discussion

• A1 is a voxel from a fully sampled 4D EPCOSI scan of healthy, fatty breast *in vivo*. B1 is the same voxel after 25% NUS of the  $k_y$ - $t_1$  plane and has significant artifacts from the large diagonal peak at (2.2ppm, 2.0ppm) obscuring the much smaller cross-peak highlighted in blue. C1 shows the MaxEnt reconstruction of B1 and has equivalent spectral peaks to the fully sampled data in A1 with the artifacts removed.

• A2, B2, and C2 show the spatial distribution of the olefinic cross peaks highlighted in blue for the fully sampled, 25% NUS, and 25% NUS with MaxEnt reconstruction from a 4D EPCOSI scan of healthy, fatty breast. B2 shows significant spatial incoherent artifacts from the NUS that are removed by MaxEnt reconstruction in C2.

• The normalized Root Mean Square Error (nRMSE) of B1/B2 is .0047 and .0014 for C1/C2.

## Conclusion

• We have shown it is possible to simultaneously NUS a spectral and a spatial dimension of an *in vivo* EPCOSI scan to 25% and successfully reconstruct the data. This acceleration translates into a clinically viable 5 minute EPCOSI scan time.

## References

- [1] Lipnick *et al*, Magn. Reson. Med. 2010; 64: 947-956 [2] Hoch & Stern, 1996, Wiley-Liss, New York [3] Skilling & Bryan, Mon. Not. Roy. Astr. Soc. 1984; 211: 111-124 [4] Daniell & Hore Mag. Res. 1989; 84: 515-536

## Acknowledgements

• DoD Idea Expansion grant for Breast Cancer Research #W81XWH-10-1-0743 and NIH training grant #5T15 LM07356

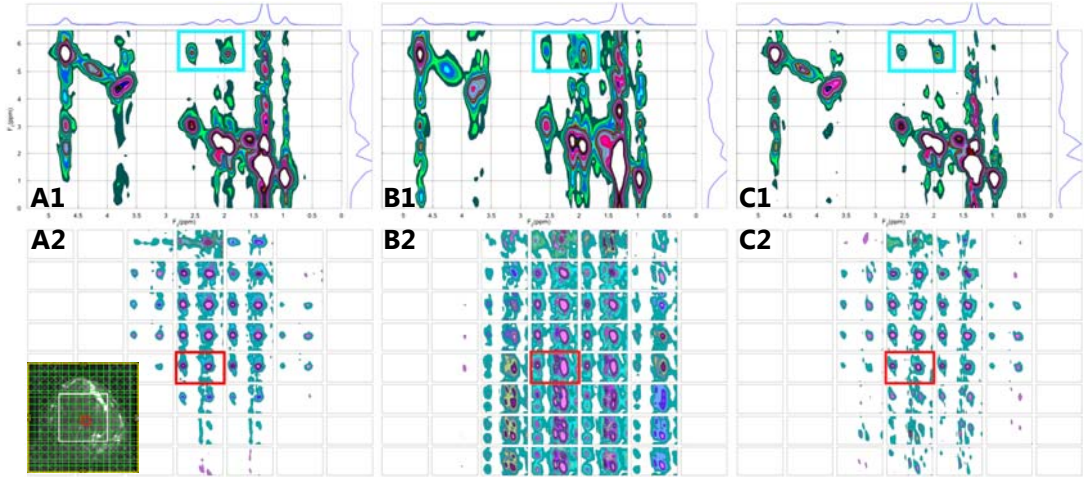


Figure 1 (Top) Selected 2D COSY spectra from a 4D EPCOSI scan of healthy, fatty breast highlighted in red in the MRI localizer image for A1) fully sampled B1) 25% NUS C1) 25% NUS with MaxEnt reconstruction. (Bottom) Spatial distribution of olefinic cross-peaks of unsaturated fatty acids highlighted in light blue for A2) fully sampled B2) 25% NUS C2) 25% NUS with MaxEnt reconstruction.

Algorithm : CAMBRIDGE MAXENT(NUS data, sample density)

High level overview of MaxEnt:  
repeat

Calculate gradients and Hessians:

$$(i) \begin{cases} g_c = \nabla_f(C), g_s = \nabla_f(S), \\ H_s = \nabla_s^2(S), H_c = \nabla_c^2(C), \\ E_s = -H_s^{-1} = \text{Entropy metric} \end{cases}$$

Calculate search directions to form basis:

$$(ii) \begin{cases} b_1 = \frac{g_s}{\|g_s\|} - \frac{g_c}{\|g_c\|} \\ b_2 = E_s g_c \\ b_3 = E_s \left( \frac{g_s}{\|g_s\|} - \frac{g_c}{\|g_c\|} \right) \\ b_4 = g_c \\ b_5 = E_s H_c E_s \left( \frac{g_s}{\|g_s\|} - \frac{g_c}{\|g_c\|} \right) \end{cases}$$

Create local 2<sup>nd</sup> order approximation from basis:

$$(iii) \begin{cases} S(y) = S(f) + y^* b^* g_s - \frac{1}{2} y^* b^* H_s b y \\ C(y) = C(f) + y^* b^* g_c + \frac{1}{2} y^* b^* H_c b y \end{cases}$$

Rotate basis to make subspace Cartesian:

$$(iv) \begin{cases} y \Rightarrow x, b^* H_s b \Rightarrow I, b^* H_c b \Rightarrow M_{diag} \\ S(x) = S_f + x^* b^* g_s - \frac{1}{2} x^* I x \\ C(x) = C_f + x^* b^* g_c + \frac{1}{2} x^* M_{diag} x \end{cases}$$

Find x that minimizes C(x) and maximizes S(x) from (iv):

$$(v) \begin{cases} x(\alpha) = \frac{M_{diag} + \alpha I}{\alpha b^* g_s - b^* g_c} \\ x = \underset{x(\alpha)}{\text{argmin}} C_f + g_s^* b x(\alpha) + \frac{1}{2} x(\alpha)^* M_{diag} x(\alpha) \end{cases}$$

Update spectrum:

$$(vi) \begin{cases} f_{old} = f_{new} + b^T x \\ \text{until stopping condition met} \\ \text{return } (F^{-1} f) \end{cases}$$

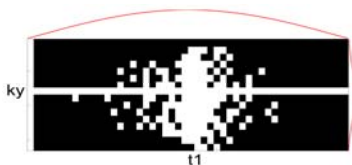


Figure 2 Poisson distributed 25% sample mask for  $k_y$  and  $t_1$  dimensions. Sample density follows sin-modulated  $t_1$  and exponentially decaying  $k_y$  signal envelopes.

## Maximum Entropy Reconstruction of Correlated Spectroscopy of Human Breast In Vivo

Brian L Burns<sup>1,2</sup>, Jon K Furuyama<sup>3</sup>, Neil Wilson<sup>3</sup>, Nicki DeBruhl<sup>3</sup>, Alex Bui<sup>2,3</sup>, and M. Albert Thomas<sup>3</sup>

<sup>1</sup>Biomedical Engineering, UCLA, Los Angeles, CA, United States, <sup>2</sup>Medical Imaging Informatics (MII), UCLA, Los Angeles, CA, United States, <sup>3</sup>Department of Radiological Sciences, UCLA

**Introduction** – The altered metabolism of breast cancer tissues gives rise to changes in metabolite concentrations that are detectable using two-dimensional (2D) Magnetic Resonance Spectroscopy (MRS) [1]. 2D Localized-Correlated Spectroscopy (L-COSY) MRS has been shown to increase the specificity and sensitivity of tumor grade classification when used with traditional techniques, such as Dynamic Contrast Enhanced (DCE)-MRI [1]. However, because of the number of  $t_1$  increments used to construct the indirect spectral dimension ( $F_1$ ), the L-COSY sequence requires on the order of 25 minutes for 100  $t_1$  increments and 8 averages [2]. To reduce scan times to a clinically acceptable 12 minutes, only 45  $t_1$  increments are typically used, but this reduces spectral resolution along  $F_1$ . Maximum entropy (MaxEnt) image reconstruction techniques have been used in Nuclear Magnetic Resonance (NMR) to non-uniformly under-sample (NUS) indirect spectral dimensions and then reconstruct the most statistically likely fully-sampled multi-dimensional spectrum [3,4]. This technique can be used to accelerate the collection of 2D L-COSY data *in vivo* by selectively under-sampling along  $t_1$ . We show that under-sampling the indirect dimension by ~50% and reconstructing the spectrum using MaxEnt preserves the metabolite diagonal peaks: olefinic fat (UFD), methyl fat (FMETD), and choline (Cho) and the cross peaks: unsaturated fatty acid, right (UFR), unsaturated fatty acid, left (UFL), and triglyceryl fat (TGFR) which have demonstrated clinical importance.

**Methods** – To qualitatively measure the performance of the MaxEnt reconstruction algorithm on NUS *in vivo* data, fully sampled 2D L-COSY scans of both healthy ( $n=10$ ) and malignant ( $n=8$ ) breast tissues were acquired on a 3T Siemens Trio scanner using the following parameters:  $1\text{cm}^3$  voxel size, TR/TE=2s/30ms, 45  $t_1$  increments, 8 averages, and no water suppression. Both scans were retrospectively under-sampled to 22 lines along the  $t_1$  dimension, apodized along the  $t_1$  and  $t_2$  dimensions, and then reconstructed using the MaxEnt algorithm to 45 lines. MaxEnt is a constrained convex optimization algorithm that uses a variant of the conjugate gradient method to iteratively solve the inverse problem [5]:

$$\text{maximize } S_{1/2}(f) \text{ s.t. } \|F^{-1}Kf - D\|_2 \leq \sigma \quad (1)$$

where  $f$  is the estimated fully-sampled spectrum at each iteration,  $F^{-1}$  is the inverse Fourier transform,  $K$  is the NUS matrix,  $D$  is the time-domain measured data,  $\sigma$  is the noise standard deviation, and  $S_{1/2}(f)$  is the spin- $\frac{1}{2}$  entropy of the estimated spectrum [3]. The spectrum with the highest entropy is that which conforms to the uniform distribution and has a flat baseline. Therefore, by maximizing the spin- $\frac{1}{2}$  entropy in (1), MaxEnt enforces sparsity of the estimated spectrum in the frequency domain and reduces incoherent aliasing artifacts in the spectrum caused by NUS. The fidelity constraint ensures that peaks in the estimated spectrum must come from the sampled data to within a tolerance of the noise. The reconstruction is performed over both dimensions simultaneously as opposed to a series of 1D reconstructions as implemented elsewhere [4].

**Results and Discussion** – Figures 1A and 1B show the 2D L-COSY spectra of the fully sampled and ~50% MaxEnt reconstruction of the NUS healthy breast tissue, respectively. As can be seen, the major diagonal and cross peaks present in healthy fatty breast tissue are present in both spectra. The peak locations, line shapes, and amplitudes of the NUS data are roughly equivalent to the fully sampled data; however a slight loss in spectral resolution along  $F_1$  is evident by the elongation of the UFR peak in the MaxEnt reconstruction. There is no corresponding loss in resolution along  $F_2$ . Figures 2A and 2B show 2D L-COSY spectra of the fully sampled and the ~50% reconstruction of the NUS malignant fatty breast tissue, respectively. The presence of water in fatty breast tissue is an indicator of breast cancer, and because of its high concentration, its broad line-width

obscures many of the cross-peaks seen in Figure 1. However, the UFR cross-peak is clearly visible in figures 2A and 2B, and the MaxEnt reconstructed peak is comparable to the fully sampled peak, even in the presence of noise. The Cho diagonal peak in figure 2, which is a sign of increased metabolic activity and malignancy, is fully resolved in the MaxEnt reconstruction and shows good agreement with the peak in the fully sampled spectrum.

**Conclusions** – We have shown that it is possible to under-sample the L-COSY sequence by up to ~50% and reconstruct *in vivo* spectra from as few as 22  $t_1$  lines that show similar spectral characteristics to spectra from fully sampled data. This acceleration translates into a sub-6 minute scan time if 8 averages are used and increases the potential use of MRS for breast cancer screening in the clinic. If increased spectral resolution is needed, the MaxEnt reconstruction is not limited to 45  $t_1$  points and can reconstruct many more NUS points than what was used in these experiments.

**References** – [1] Lipnick, et al., NMR Biomed. 2010; 23: 922-930 [2] Thomas, et al., Mag. Res. Med. 2001; 46:58-67 [3] Daniell & Hore, J. Mag. Res. 1989; 84: 515-536 [4] Hoch & Stern, 1996, Wiley-Liss, New York [5] Skilling & Bryan, Mon. Not. Roy. Astr. Soc. 1984; 211: 111-124

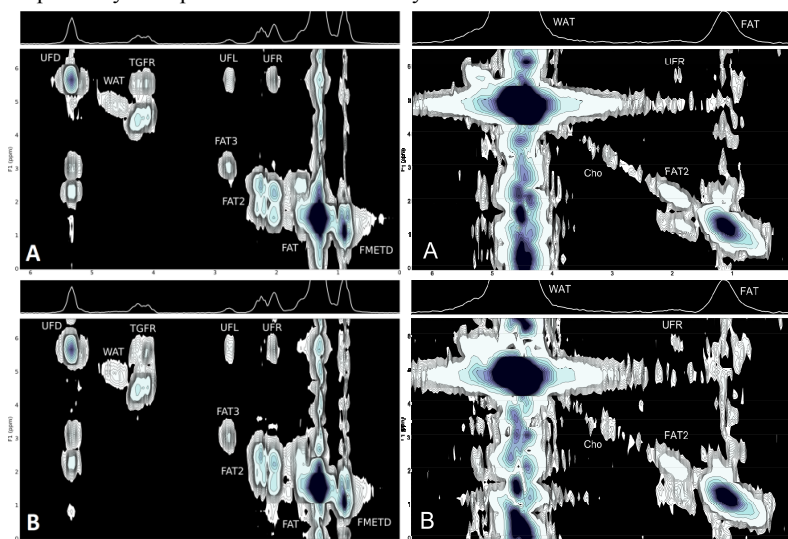


**Fig 2:** *in vivo* 2D L-COSY spectra of a 25 year old healthy fatty breast tissue (A) fully sampled along  $t_1$  (B) 50% reconstruction along  $t_1$

**Fig 2:** *in vivo* 2D L-COSY spectra of a 55 year old malignant tumor in fatty breast tissue (A) fully sampled along  $t_1$  (B) 50% reconstruction along  $t_1$

**Acknowledgements** – DoD Idea Expansion grant for Breast Cancer Research #W81XWH-10-1-0743 and NIH training grant #5T15 LM07356

# Maximum Entropy Based Reconstruction of Echo-Planar Correlated Spectroscopic Imaging of Human Breast In Vivo

Brian Burns<sup>1,2</sup>, Jon K Furuyama<sup>3</sup>, Neil Wilson<sup>4</sup>, Nicki DeBruhl<sup>4</sup>, and M. Albert Thomas<sup>2</sup>

<sup>1</sup>Department of Radiological Sciences, UCLA, Los Angeles, CA, United States, <sup>2</sup>Medical Imaging Informatics (MII), UCLA, <sup>3</sup>Radiological Sciences, UCLA, <sup>4</sup>Department of Radiological Sciences, UCLA

**Introduction** – 2D Localized Correlated Spectroscopy (L-COSY) has been shown to be a powerful tool in the detection of breast cancer but is limited to a single voxel [1]. The recently introduced Echo-Planar based Correlated Spectroscopic Imaging (EPCOSI) sequence allows for the simultaneous acquisition of two spatial ( $k_y$ ,  $k_x$ ) and two spectral ( $t_2$ ,  $t_1$ ) dimensions in a single experiment [2]. The 4D EPCOSI sequence interleaves the acquisition of the  $k_x$  and  $t_2$  dimensions along the EPI read-out, while  $k_y$  and  $t_1$  lines are incrementally acquired as indirect dimensions, requiring 20 minutes for a typical scan. To reduce scan times using standard Fast Fourier Transform (FFT) based reconstruction techniques would require the reduction of either the  $k_y$  spatial or  $t_1$  spectral dimensions, and a corresponding reduction in resolution. Maximum entropy (MaxEnt) image reconstruction techniques have been used in Nuclear Magnetic Resonance (NMR) to non-uniformly under-sample (NUS) indirect spectral dimensions and in imaging to NUS spatial dimensions then reconstruct the fully-sampled multi-dimensional spectra or image [3,4,5]. This technique can be used to accelerate the collection of 4D EPCOSI data *in vivo* by selectively under-sampling along  $k_y$  and  $t_1$ . We show that under-sampling the indirect dimensions by ~25% and reconstructing the spatially localized EPCOSI spectra using MaxEnt preserves the spatial distribution of the metabolite diagonal peaks found in healthy breast tissue and reduces the scan time to 5 minutes.

**Methods** – An EPCOSI scan of healthy breast was performed on a 3T Siemens Trio scanner with the following parameters:  $1 \times 1 \times 2 \text{ cm}^3$  voxel size, TR/TE=1.5s/30ms, 50  $t_1$  increments,  $16 \times 16 \text{ cm}^2$  FOV, 1 average with water suppression and 2 averages without water suppression. The scan was retrospectively under-sampled to ~25% of the  $k_y$ - $t_1$  plane, using the map in Fig. 1. The NUS spatial and spectral dimensions were simultaneously reconstructed using MaxEnt. The MaxEnt algorithm uses a variant of the conjugate gradient method to iteratively solve the constrained convex optimization problem [5]:

$$\text{maximize } S_{1/2}(f) \text{ s.t. } \|F^{-1}Kf - D\|_2 \leq \sigma \quad (1)$$

where  $f$  is the estimated fully-sampled spatially distributed spectra at each iteration,  $F^{-1}$  is the inverse Fourier transform,  $K$  is the NUS matrix,  $D$  is the time-domain measured data,  $\sigma$  is the noise standard deviation, and  $S_{1/2}(f)$  is the spin- $1/2$  entropy of the estimated spectra [3]. The spatially distributed spectra with the highest entropy are those which conform to the uniform distribution and have a flat baseline. Therefore, by maximizing the spin- $1/2$  entropy in (1), MaxEnt enforces sparsity of the estimated spectra in the frequency and  $k$ -space domains and reduces incoherent aliasing artifacts in the spectra caused by NUS. The fidelity constraint ensures that peaks in the estimated spectra and their spatial distribution must come from the sampled data to within a tolerance of the noise. The reconstruction is performed over all dimensions simultaneously as opposed to a series of 1D reconstructions as implemented elsewhere [5].

**Results and Discussion** – Figures 2A and 2B show the fully sampled and 25% MaxEnt reconstruction of the selected 2D COSY spectra from a voxel of healthy fatty breast tissue. As can be seen, the spectral characteristics of the NUS data with MaxEnt reconstruction are equivalent to the fully sampled data; the same diagonal and cross peaks are present in both spectra without a significant increase in noise. Figures 3A and 3B show the spatial distribution of the olefinic cross peak selected in Figure 2 for the fully sampled and 25% MaxEnt reconstructed 4D EPCOSI of healthy fatty breast tissue. The spatial distributions between the fully sampled and MaxEnt reconstruction show very good agreement, with the exception of some spatial bleeding on the outer edges of the distribution.

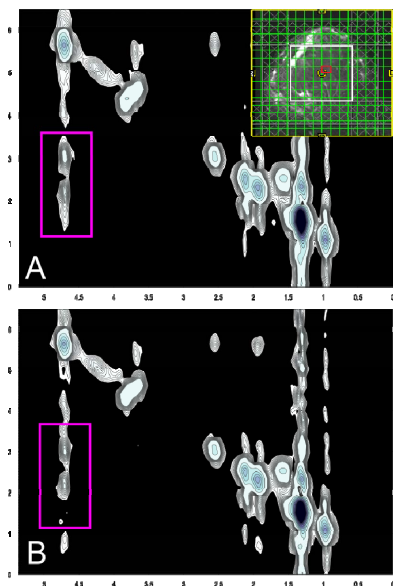


**Figure 2:** Selected 2D COSY spectra of healthy fatty breast tissue highlighted in red for A) fully sampled and B) 4x under-sampled with MaxEnt reconstruction.

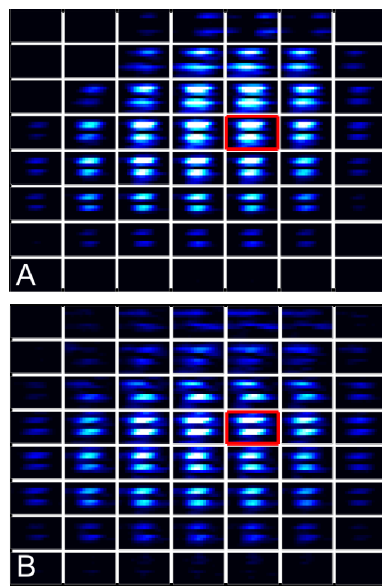


**Figure 3:** Spatial distribution of Olefinic cross-peaks highlighted in purple in Fig. 2 for A) fully sampled and B) 4x under-sampled with MaxEnt reconstruction.

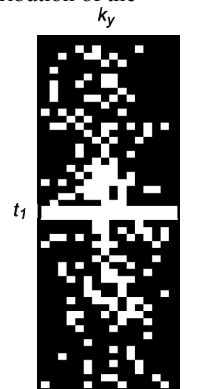


**Figure 1:** 4x under-sampling mask for  $k_y$  and  $t_1$  dimensions. White points are sampled.

**Conclusions** – We have shown that it is possible to under-sample both the spectral and spatial dimensions of an *in vivo* EPCOSI sequence by up to 25% and reconstruct the spectra with similar spatial distributions and spectral characteristics to the fully sampled data. This acceleration translates into a 5 minute EPCOSI scan time and increases the potential use of 4D MRS in the clinic. Compressed Sensing (CS)-based reconstruction can be used alternatively for processing the NUS EPCOSI data. Further research regarding the merits and demerits of the two reconstruction methods is in progress.

**References** – [1] Lipnick, et al., NMR Biomed. 2010; 23: 922-930 [2] Lipnick *et al*, Magn. Reson. Med. 2010; 64: 947-956 [3] Skilling & Bryan, Mon. Not. Roy. Astr. Soc. 1984; 211: 111-124 [4] Daniell & Hore Mag. Res. 1989; 84: 515-536 [5] Hoch & Stern, 1996, Wiley-Liss, New York [6] Donoho, IEEE Trans Info Theory. 2006; 52: 1289-1306 [7] Lustig *et al*, Magn. Reson. Med. 2007; 58:1182-1195

**Acknowledgements** – DoD Idea Expansion grant for Breast Cancer Research #W81XWH-10-1-0743 and NIH training grant #5T15 LM07356



**Maximum Entropy Reconstruction of Non-Uniformly Under-Sampled Multidimensional Spectroscopic Imaging in vivo**

Journal:	<i>Magnetic Resonance in Medicine</i>
Manuscript ID:	MRM-12-13731
Wiley - Manuscript type:	ISMRM Young Investigator Award
Date Submitted by the Author:	11-Oct-2012
Complete List of Authors:	Burns, Brian; UCLA School of Medicine, Biomedical Engineering Wilson, Neil; David Geffen School of Medicine, Radiology Furuyama, Jonathan; David Geffen School of Medicine, Radiology Thomas, M. Albert; David Geffen School of Medicine, Radiology
Research Type:	Reconstruction < Technique Development < Technical Research, Spectroscopy/Spectroscopic Imaging < Technique Development < Technical Research
Research Focus:	No specific tissue or organ focus

SCHOLARONE™  
Manuscripts

1  
2  
3  
4  
5  
6  
7  
8  
9  
10  
11  
12  
13  
14  
15  
16  
17  
18  
19  
20  
21  
22  
23  
24  
25  
26  
27  
28  
29  
30  
31  
32  
33  
34  
35  
36  
37  
38  
39  
40  
41  
42  
43  
44  
45  
46  
47  
48  
49  
50  
51  
52  
53  
54  
55  
56  
57  
58  
59  
60

## Maximum Entropy Reconstruction of Non-Uniformly Under-Sampled Multidimensional Spectroscopic Imaging in vivo

Brian Burns<sup>1,2</sup>, Neil E. Wilson<sup>1,3</sup>, Jon K. Furuyama<sup>1,3</sup>, M. Albert Thomas<sup>1,2,3</sup>

<sup>1</sup> Department of Radiological Sciences, David Geffen School of Medicine, University of California, Los Angeles, California, USA

<sup>2</sup> Department of Biomedical Engineering, University of California, Los Angeles, California, USA

<sup>3</sup> Biomedical Physics IDP, University of California, Los Angeles, California, USA

**Running Title:** MaxEnt Reconstruction of Under-sampled MRSI Containing 2D Spectral Combined with 2D Spatial in vivo

**Word Count:** 5333

**Address for Correspondence:**

M. Albert Thomas Ph.D.  
Radiological Sciences  
David Geffen School of Medicine at UCLA  
10833 Le Conte Avenue  
Los Angeles, CA 90095-1721  
Tel: (310) 206 4191  
Fax: (310) 825 5837  
Email: [athomas@mednet.ucla.edu](mailto:athomas@mednet.ucla.edu)

## Abstract

**Purpose:** To reduce scan times of 4D Magnetic Resonance Spectroscopic Imaging by applying non-uniform under-sampling (NUS) to the indirectly acquired dimensions ( $k_y$  and  $t_1$ ) and reconstructing those dimensions using Maximum Entropy (MaxEnt) iterative reconstruction.

**Methods:** Simulated and in vivo 4D Echo-Planar based Correlated Spectroscopic Imaging (EP-COSI) data were retrospectively under-sampled, and in vivo 4D Echo-Planar J-Resolved Spectroscopic Imaging (EP-JRESI) prostate data was prospectively undersampled in the  $k_y$ - $t_1$  plane. The under-sampled data sets were reconstructed using the Cambridge iterative algorithm to solve the MaxEnt reconstruction problem.

**Results:** Simulated data reconstructions demonstrated the MaxEnt reconstruction improves data fidelity considerably over the under-sampled data at SNRs from 2 to 20 and percent under-samplings of 20 to 80%. 25% NUS was applied retrospectively to EP-COSI and prospectively to EP-JRESI in vivo data. The NUS EP-COSI and EP-JRESI in vivo data were under-sampled to 25% and the incoherent artifacts caused by the under-sampling were successfully removed by the MaxEnt reconstruction.

**Conclusion:** MaxEnt reconstruction preserved the spectral-spatial resolution of the non-uniformly under-sampled data and reduced EP-JRESI scan times from 24 to 6 minutes in human prostate and can potentially reduce EP-COSI scan times from 20 to 5 minutes in human breast.

**Keywords:** EP-COSI, EP-JRESI, Maximum Entropy, Non-Uniform Under-Sampling, Spectroscopy, Spectroscopic Imaging

## INTRODUCTION

The altered metabolism of cancer gives rise to changes in metabolite concentrations that can potentially be detected non-invasively using one-dimensional (1D) magnetic resonance spectroscopy (MRS) in vivo [1,2,3,4,5]. However, the overlap of spectral peaks in 1D MRS is a major concern for identifying individual metabolites. Two dimensional (2D) MRS has increased spectral dispersion over 1D MRS and can disentangle over-lapping complex spectral peaks [6]. Single voxel 2D MRS has been shown to increase the specificity and sensitivity of tumor grade classification when used with traditional techniques, such as dynamic contrast enhanced (DCE)-MRI in the breast [7] and the Gleason grading system in the prostate [8]. However, requiring multiple  $t_1$  increments per voxel to form the second spectral dimension limits its ability to provide multi-voxel coverage due to long scan times needed to combine two spectral and two spatial dimensions.

With the advent of Echo-Planar Spectroscopic Imaging (EPSI), magnetic resonance spectroscopic imaging (MRSI) scans with one spectral dimension could be completed within clinically acceptable times by interleaving the acquisition of a spatial and spectral dimension within the EPSI readout [9] [10] [11]. The recently introduced Echo-Planar based Correlated Spectroscopic Imaging (EP-COSI) [12] and Echo-Planar J-Resolved Spectroscopic Imaging (EP-JRESI) [13] sequences allow for the simultaneous acquisition of two spatial ( $k_y$ ,  $k_x$ ) and two spectral ( $t_2$ ,  $t_1$ ) dimensions in a single recording to form 4D MRSI. Both sequences interleave the acquisition of the  $k_x$  and  $t_2$  dimensions within the EPSI read-out, but  $k_y$  and  $t_1$  are incrementally acquired as indirect dimensions during each TR. The EP-COSI and EP-JRESI sequences have the benefits of increased spectral dispersion and multi-voxel support; however their scan times are directly proportional to the number of increments in the  $k_y$  and  $t_1$  dimensions and can take 20 to 40 minutes using typical parameters which is too long to be used for a routine clinical protocol [12] [13].

When using the Fast Fourier Transform (FFT), reducing 4D EP-COSI and EP-JRESI scan times requires the reduction of either the  $k_y$  spatial or  $t_1$  spectral dimensions through truncation or lower sampling rates, and a corresponding unwanted reduction in resolution

1  
2  
3 or bandwidth with the potential for aliasing. However, non-uniform under-sampling of  
4 the spatial-spectral  $k_y$ - $t_1$  plane in combination with iterative non-linear reconstruction  
5 techniques can be used to accelerate the collection of 4D MRSI data in vivo while  
6 preserving the spatial and spectral resolution [14].  
7  
8  
9

10  
11  
12 Earlier work has demonstrated the feasibility of under-sampling the mixed-domain  $k_y$ - $t_1$   
13 plane of a 4D EP-JRESI data set and reconstructing the missing points with Compressed  
14 Sensing (CS) [14], a popular method of under-sampled iterative image reconstruction that  
15 promotes data sparsity in the reconstruction domain and data fidelity in the sample  
16 domain [15] [16]. The nature of spatial-spectral incoherent artifacts in the  $k_y$ - $t_1$  plane  
17 were explored, and it was shown that  $l_1$ -norm-based CS reconstruction is a viable means  
18 of reducing the scan times of 4D EP-JRESI in vivo through under-sampling. In recent  
19 years, CS reconstruction has been successfully applied to under-sampled MRI [17] [18],  
20 3D MRSI [19], dynamic MRI [20] [21], and a number of other promising applications not  
21 necessarily related to medical imaging [22] [23].  
22  
23  
24  
25  
26  
27  
28  
29  
30

31  
32 Maximum Entropy (MaxEnt) image reconstruction is an alternative non-linear iterative  
33 reconstruction technique to CS. It promotes the entropy of the data in the reconstruction  
34 domain while preserving data fidelity in the sample domain [24,25]. MaxEnt has been  
35 successfully applied to under-sampled images in astronomy and multi-dimensional  
36 spectra in NMR [25] [26] [27]. However, MaxEnt has not been applied to the mixed-  
37 domain  $k_y$ - $t_1$  plane of a 4D MRSI data set in vivo.  
38  
39  
40  
41  
42  
43

44  
45 In information theory, entropy is a measure of the uncertainty of a variable state and the  
46 probability of its occurrence; the more uncertain its state, the higher its entropy. States  
47 that are all equally likely and whose probabilities conform to the uniform distribution  
48 have the maximum possible entropy [28]. Entropy in MRSI represents a measure of the  
49 phase coherence of an ensemble of spins within a given voxel volume [26]. Normalized  
50 for the concentration of spins within the volume, high-amplitude NMR signals represent  
51 states of full phase coherence and low entropy, while low amplitude NMR signals  
52 represent states of low phase coherence and high entropy. If the phase distribution  
53  
54  
55  
56  
57  
58  
59  
60

1  
2  
3 conforms to a state of low phase coherence, such as a uniform distribution, the entropy is  
4 maximized as it is in information theory. Therefore, by maximizing the entropy of the  
5 spatial, spectral-domain in MaxEnt, under-sampling artifacts are removed from the  
6 reconstruction because they represent states of high phase coherence and low entropy that  
7 are not present in the sampled data.  
8  
9

10  
11  
12  
13  
14 In this paper, we show that MaxEnt reconstruction is a viable technique to reduce scan  
15 times by successfully reconstructing under-sampled 4D MRSI data. We quantitatively  
16 characterize the MaxEnt reconstruction by showing results for retrospectively under-  
17 sampled simulated 4D EP-COSI data at varying levels of SNR and percent under-  
18 sampling. Additionally, we show that under-sampling the  $k_y$ - $t_1$  plane to 25% and using  
19 MaxEnt to reconstruct an in vivo 4D EP-COSI data set retrospectively and an in vivo EP-  
20 JRESI data set prospectively preserves the spatial-spectral resolution of the spectra and  
21 reduces scan times to 5 minutes in the breast and 6 minutes in the prostate using typical  
22 parameters.  
23  
24  
25  
26  
27  
28  
29

## 30 31 **METHODS**

### 32 33 **MR Simulations**

34  
35  
36 The effects of SNR and percent under-sampling on the MaxEnt reconstruction were  
37 quantitatively assessed using a noise-free simulated 4D EP-COSI data set that contained  
38 either N-acetylaspartate (NAA), creatine (Cr), choline (Cho), lactate (Lac), or nothing in  
39 each voxel, as represented in the top of Figure 1 by a diagonal peak from each metabolite.  
40 Each metabolite was simulated using the GAMMA NMR libraries [29] from a Localized  
41 2D Correlated Spectroscopy (L-COSY) sequence [30] with the following parameters: 100  
42  $t_1$  increments, 1024 points in  $t_2$ , TR/TE= 1.5s/30ms, and spectral bandwidths of 1250Hz  
43 and 2000Hz along  $F_1$  and  $F_2$ , respectively. Each 2D spectrum was line-broadened by 1 Hz  
44 and apodized by a sine-squared filter along  $t_1$  and a skewed sine-squared filter with skew  
45 parameter 0.5 along  $t_2$ . They were then copied into an 8x8 spatial grid to simulate  
46 spatially distributed metabolites as follows: the upper left quadrant contained 2x2 voxels  
47 of NAA, the upper right quadrant contained 2x2 voxels of Cr, the lower left quadrant  
48 contained 2x2 voxels of Cho, and the lower right quadrant contained 2x2 voxels of Lac.  
49  
50  
51  
52  
53  
54  
55  
56  
57  
58  
59  
60

As a result of under-sampling the  $k_y$ - $t_1$  plane, the spatial-spectral artifacts caused the NAA and Cho voxels to alias into each other and the Cr and Lac voxels to alias into each other, as shown in the bottom of Figure 1. This changed the NAA to Cho and Lac to Cr ratios as the spatial and spectral separation between the metabolites broke down.

The simulated 4D EP-COSI data set was retrospectively reconstructed using MaxEnt at 20, 40, 60 and 80% under-sampling and SNRs of 2 to 20 in increments of 2. The SNR was varied by simulating different levels of thermal noise in the data set by adding Gaussian noise in quadrature to the noise-free 4D EP-COSI data set as in [31]. The desired SNR was achieved by ensuring the Root Mean Square (RMS) of the additive noise was equal to  $1/SNR$  of the noise-free data set RMS, such that:

$$\text{noisy data} = \text{noise free} + \frac{\text{RMS}(\text{Noise Free})}{\text{RMS}(\text{Noise}) * \text{SNR}} * \text{Noise} \quad [1]$$

Because the additive noise was random, each SNR was simulated and reconstructed 20 times per sample mask to account for random fluctuations in the reconstruction. The sampling masks were created using the 2D Poisson-gap method described below.

### MR Spectroscopic Imaging

A 4D EP-COSI scan of a 34 year old healthy human breast was acquired on a Siemens 3T Trio scanner with the following parameters:  $1 \times 1 \times 1 \text{ cm}^3$  voxel size, 50  $t_1$  increments, TR/TE/averages = 1.5s/30ms/1, a  $16 \times 16 \text{ cm}^2$  FOV, and spectral bandwidths of 1250Hz and 1190Hz along  $F_1$  and  $F_2$ , respectively. The scan was fully sampled and took 20 minutes to complete. Prior to being under-sampled and reconstructed, coil combination and eddy current correction were applied to the fully sampled data set. It was then apodized by a sine-squared filter along  $t_1$  and a skewed sine-squared filter with skew parameter 0.5 along  $t_2$ . The fully sampled data set was then retrospectively under-sampled to 25% in the  $k_y$ - $t_1$  plane using the mask shown in Figure 4 and reconstructed by MaxEnt.

1  
2  
3  
4  
5 The prospective MaxEnt reconstruction was performed on a 4D EP-JRESI scan of a 71  
6 year old human prostate with cancerous tumors in the left and right base (Gleason score  
7 of 3+3, prostatic specific antigen of 8). The scan was acquired on a Siemens 3T Trio  
8 scanner using the single-channel endorectal coil with the same parameters as the EP-  
9 COSI breast scan except 64  $t_1$  increments and a spectral bandwidth of  $\pm 500$ Hz along  $F_1$   
10 was used. The  $k_y$ - $t_1$  mask shown in Figure 5 was used during the scan to acquire 25% of  
11 the  $k_y$ - $t_1$  plane during the acquisition. Eddy current correction was applied to the 4D  
12 prostate data after MaxEnt reconstruction.  
13  
14  
15  
16  
17  
18  
19

### 20 **Sample Mask Generation**

21  
22 The 2D Poisson-gap sample masks used were derived from 1D Poisson-gap sample  
23 masks [32]. Poisson-gap sample masks avoid large gaps between samples, which are  
24 detrimental to the reconstruction, while ensuring the samples are randomly distributed  
25 [33].  
26  
27  
28  
29  
30  
31

32 The effects of the sample mask on the SNR and line-shape of spectral reconstructions are  
33 well documented [33] [34] [35]. Sample masks that follow the time-domain NMR signal  
34 envelope and sample more points at higher SNR have lower RMS errors (RMSE) and  
35 non-linearity compared to sample masks that do not. Because the  $t_1$  dimension in a  
36 filtered EP-COSI scan has a sine-bell signal envelope and the  $t_1$  dimension in an EP-  
37 JRESI scan has an exponentially decaying signal envelope, the 2D Poisson-gap sample  
38 masks were modulated along  $t_1$  with sine or exponential decay functions, respectively.  
39 The  $k_y$  dimension for both scan types was modulated by an exponential decay function  
40 similarly to what has been used previously to maximize spatial SNR [36].  
41  
42  
43  
44  
45  
46  
47  
48

49 The rate parameter,  $\lambda$ , determines both the mean and variance of a Poisson distribution.  
50 The probability of generating a sample gap,  $g$ , from a Poisson distribution is  
51 characterized by:  
52  
53

$$54 \quad p(g, \lambda) = \lambda^g \cdot e^{-\lambda} / g! \quad [2]$$

55  
56  
57  
58  
59  
60

For large  $\lambda$ , large values of  $g$  are more likely, and for small  $\lambda$ , small values of  $g$  are more likely. Therefore, the probability of  $g$  can be modulated by varying the value of  $\lambda$  according to a sine or exponential decay function, and the probability of small gaps can be increased where the SNR is highest in the MR signal envelope [32]. To generate  $g$  as a function of  $\lambda$ , a Poisson process can be simulated using various techniques that do not depend on *a priori* knowledge of  $g$  as above [37]. For these experiments, the *poissrnd*( $\lambda$ ) function in Matlab was used to generate  $g$  as a function of  $\lambda$ . It takes as input an array of  $\lambda$  and returns an array of sample gaps with local mean and variance,  $\lambda$ .

An example of the 2D  $\lambda$ , gap, and mask arrays generated by Poisson-gap mask creation are shown in Figure 2 and illustrates their relationships; as the size of  $\lambda$  and the gaps increase, the sample density decreases in that area of the mask. The magnitude Point Spread Function (PSF) of each mask is shown and demonstrates the viability of this approach; the single dominant central peak with small side-lobes, surrounded by low amplitude, incoherent artifacts is the desired profile of a random under-sampling mask PSF [38] [39].

#### 4D MaxEnt Reconstruction

MaxEnt image reconstruction was used in these experiments to reconstruct the under-sampled data sets. MaxEnt reconstruction maximizes the entropy of the data in the spatial, spectral-domain while maintaining data fidelity with the sampled data in the k-space, time domain [25].

MaxEnt image reconstruction of 4D MRSI data is formulated as a constrained convex optimization problem [25] [27]:

$$\begin{aligned} & \text{maximize } S(m)_{1/2} \\ & \text{s. t. } \|K\mathcal{F}m - d\|_2^2 \leq C_0 \end{aligned} \quad (3)$$

where  $m = (y, x, F_2, F_1)$  is the reconstructed spatial, spectral-domain data,  $\mathcal{F}$  is the 4D Fourier operator,  $K$  is the under-sampling mask that determines which samples were acquired in the  $k_y$ - $t_1$  plane,  $d = (k_y, k_x, t_2, t_1)$  is the k-space, time-domain sampled data,  $C_0$  is the standard deviation of the noise in  $d$ , and  $S(m)_{1/2}$  is the entropy of the estimated spectrum

The entropy used in these experiments was not the often used  $-\sum p \log(p)$  entropy introduced by Shannon [28] but the  $S_{1/2}$  entropy derived by Daniell and Hore specifically for NMR spectra originating from spin  $1/2$  nuclei, such as  $^1\text{H}$  used in MRSI [26]:

$$S(m)_{\frac{1}{2}} = - \sum \frac{|m|}{def} \log \left( \frac{|m|/def + \sqrt{4 + \left(\frac{|m|}{def}\right)^2}}{2} \right) - \sqrt{4 + \left(\frac{|m|}{def}\right)^2} \quad (4)$$

where  $def$  is a scaling parameter related to the sensitivity of the scanner and is calculated

for  $m$  of length  $N$  as  $\sqrt{C_0/N}$  [27]. The underlying physical processes that produce an MR

spectrum are not based on particle, or discrete events so they cannot be modeled by simple Poisson processes as required for the derivation of Shannon entropy [40]. They are governed by the density matrix of the spin system under investigation. This equation can be applied to any MR spectrum originating from spin  $1/2$  nuclei and addresses previous concerns regarding the use of entropy in MRS and MRI reconstruction [41].

The MaxEnt reconstruction problem was solved by a Matlab implementation of the Cambridge algorithm [25]. It recasts MaxEnt image reconstruction into an unconstrained convex optimization problem and uses a variant of the conjugate gradient method to iteratively find the extrema in two phases; the first phase minimizes the fidelity constraint, and the second phase maximizes the entropy, while keeping the fidelity constraint minimized. The stopping criterion for the problem is reached when the gradients of the entropy,  $S(m)$ , and fidelity constraint,  $C(m)$ , are parallel:  $\left| \frac{\nabla S}{\|S\|_2} - \frac{\nabla C}{\|C\|_2} \right| <$

.001. Specific details on the algorithm and modifications to accommodate multidimensional MR data can be found in [27].

## RESULTS

### MR Simulations

Quantitative results for the MaxEnt reconstruction of the simulated 4D EP-COSY data set at different percent under-samplings and SNR are shown in Figure 3. As described earlier, noise was added to the noiseless 4D data set in order to simulate SNRs of 2 through 20 in increments of 2 which were then undersampled to 80%, 60%, 40%, and 20% and reconstructed by MaxEnt. This was repeated 20 times per SNR and percent under-sampling in order to produce a mean and standard deviation for each metric.

The left pane of Figure 3 shows the average RMSE versus SNR for the under-sampled and MaxEnt reconstructed data sets at each percent under-sampling. The RMSE provides an estimate of reconstruction accuracy with respect to a reference data set that increases as the two data sets become more dissimilar. The RMSE was calculated in the spatial-spectral domain as:

$$RMSE = \frac{1}{N} \sqrt{\sum (|data| - |full|)^2} \quad (5)$$

where  $N$  is the number of data points,  $full$  is the fully sampled data set, and  $data$  is the under-sampled or MaxEnt reconstructed data set. Error bars are not shown because the standard deviations were three to four orders of magnitude smaller than the mean RMSEs and did not vary noticeably over percent under-sampling or SNR. As can be seen, the RMSE of the under-sampled data set increases as the percent of sampled data decreases but does not vary considerably with SNR. The MaxEnt reconstructions decrease the RMSE significantly at each SNR and percent under-sampling compared to the under-sampled data set but begin to rise at very low SNR.

The right pane of Figure 3 shows the average NAA to Cho and Lac to Cr ratios versus SNR for the fully sampled, under-sampled, and MaxEnt reconstructed data sets at 80%, 60%, 40%, and 20% under-sampling. The ratios were calculated from the peak integrated

1  
2  
3 areas of each metabolite at the ppm locations listed in Table 1 and then normalized by the  
4 fully sampled ratios at SNR=20. Each peak area was calculated only over the four  
5 spatially distributed voxels for each metabolite. Therefore, the NAA peak area was  
6 calculated over voxels (2,2), (2,3), (3,2) and (3,3) as shown in Figure 1, for example. This  
7 ensured that any spectral-spatial leakage caused by the under-sampling into adjacent  
8 voxels would modify the peak area for each metabolite and change the metabolite ratios  
9 as their peaks aliased along the  $k_y$ - $t_1$  plane.  
10  
11  
12  
13  
14  
15  
16

17  
18 The NAA/Cho and Lac/Cr ratios for the under-sampled data set shown in the bottom of  
19 the right pane in Figure 3 differ noticeably from the fully sampled ratios at each SNR.  
20 The NAA/Cho ratios are 1-8% larger than the fully sampled ratios and increase as the  
21 percent under-sampling decreases. The Lac/Cr ratios decrease as less data is sampled and  
22 are up to 9% lower than the fully sampled ratios for sample rates of 80, 60, and 40%, and  
23 17% lower for the 20% sample rate. Both the NAA/Cho and Lac/Cr ratios show  
24 significant deviations in the metabolite ratios compared to the fully sampled true ratios;  
25 however, these deviations are limited to the percent under-sampling and are not largely  
26 affected by SNRs down to 2.  
27  
28  
29  
30  
31  
32  
33  
34

35  
36 The MaxEnt reconstruction ratios for NAA/Cho and Lac/Cr shown in the top of the right  
37 pane in Figure 3 show much better agreement with the fully sampled ratios at each SNR  
38 and percent under-sampling than the under-sampled data. The NAA/Cho ratios are within  
39 1% of the fully sampled ratios at SNRs greater than 6 but do deviate as high as 3% for  
40 lower SNRs. The Lac/Cr ratios are also improved across all SNRs to be within 5% of the  
41 fully sampled ratios for sample rates of 80, 60, and 40% and 12% for the 20% sample  
42 rate; however, unlike the NAA/Cho ratios, the Lac/Cr ratios were affected by decreasing  
43 SNR and improvements over the under-sampled data set are less significant at SNRs less  
44 than 6.  
45  
46  
47  
48  
49  
50  
51

### 52 **Retrospective Under-sampling of 4D EP-COSY**

53

54  
55 The results from retrospectively under-sampling to 25% and then MaxEnt reconstructing  
56 a fully sampled 4D EP-COSY scan of healthy breast in vivo are shown in Figure 4. The  
57  
58  
59  
60

1  
2  
3 mask used to under-sample the  $k_y$ - $t_1$  plane is shown on the far left along with the signal  
4 envelopes for each dimension and was generated using the 2D Poisson-gap method  
5 described earlier in this paper. The central point in  $k_y$  was sampled for each  $t_1$  increment  
6 and the 1<sup>st</sup>  $t_1$  point was sampled at each  $k_y$ . [35] [17]. Because it is a 4D data set where  
7 each voxel is a 2D spectrum, space limitations prevent us from showing every voxel in  
8 the 16x16 FOV. Therefore, only a selected 2D COSY spectrum from the data set as well  
9 as the spatial distribution of specific spectral peaks is shown.  
10  
11  
12  
13  
14  
15

16  
17 Figure 4 A1 shows a 2D COSY spectrum extracted from the fully sampled 4D EP-COSI  
18 scan of healthy breast in vivo. It was taken from the fatty breast region highlighted in  
19 Figure 4 A2. It clearly shows the lipid diagonal peaks: olefinic fat (UFD), methyl fat  
20 (FMETD), and fat (FAT/FAT2/FAT3) and the cross peaks: unsaturated fatty acid right  
21 (UFR), unsaturated fatty acid left (UFL), and triglyceryl fat (TGFR) [7]. The spatial  
22 distribution of the UFL and UFR cross-peaks from the fully sampled 4D EP-COSI scan is  
23 shown in Figure 4 A2 overlaid on the anatomical MRI.  
24  
25  
26  
27  
28  
29  
30

31 Figure 4 B1 shows the same 2D COSY spectrum as Figure 4 A1 after 25% under-  
32 sampling has been applied to the  $k_y$ - $t_1$  plane using the mask shown at left. The spatial-  
33 spectral incoherent artifacts from the under-sampling manifest as smeared peaks along  $t_1$ ,  
34 which is illustrated by the collapse of the peaks in the 1D projection along the  $F_1$   
35 dimension on the right. The aliasing of the large diagonal fat peaks around ( $F_2=2\text{ppm}$ ,  
36  $F_1=2\text{ppm}$ ) obscure the much smaller UFL and UFR cross-peaks around ( $F_2=2.1\text{ppm}$ ,  
37  $F_1=5.4\text{ppm}$ ). Figure 4 B2 shows the spatial distribution of the UFL and UFR cross-peaks  
38 and how spatial artifacts from under-sampling  $k_y$ - $t_1$  manifest as errant peaks in adjacent  
39 voxels when compared to the distribution of fully sampled peaks in Figure 4 A2.  
40  
41  
42  
43  
44  
45  
46  
47

48 Figure 4 C1 shows the 2D COSY spectrum from Figure 4 B1 after MaxEnt  
49 reconstruction has been applied. The majority of spectral artifacts seen in Figure 4 B1  
50 have been removed and the metabolite peaks have been rebuilt in the 1D projection on  
51 the right of the figure. The aliasing caused by the diagonal fat peaks around ( $F_2=2\text{ppm}$ ,  
52  $F_1=2\text{ppm}$ ) has been removed and the UFL and UFR cross-peaks around ( $F_2=2.1\text{ppm}$ ,  
53  
54  
55  
56  
57  
58  
59  
60

1  
2  
3  $F_1=5.4\text{ppm}$ ) are fully resolved. When compared to the fully sampled spectrum in Figure 4  
4 A1, the MaxEnt reconstructed spectrum has equivalent spectral peaks, and all of the  
5 significant diagonals and cross-peaks are fully resolved. The errant peaks in the spatial  
6 distribution in Figure 4 B2 caused by the spatial under-sampling have been removed in  
7 Figure 4 C2.  
8  
9  
10  
11

12  
13 The range of values for the  $(\text{UFL}+\text{UFR})/(\text{FAT3}+\text{FAT2})$  integrated peak area ratio and  
14 average error from the fully sampled ratios for all 24 voxels in the localized VOI is  
15 shown in Table 2 for the under-sampled and MaxEnt reconstructed data sets. As can be  
16 seen, under-sampling caused the ratios to vary considerably from the fully sampled ratios  
17 with a high mean ratio error. The MaxEnt reconstructed ratios show much better  
18 agreement with the fully sampled ratios and have a much smaller mean ratio error.  
19  
20  
21  
22  
23  
24

### 25 **Prospectively Undersampled 4D EP-JRESI**

26  
27 The results from the prospectively under-sampled 4D EP-JRESI scan of a human prostate  
28 with malignant lesions in the left and right base are shown in Figures 5 and 6. The 25%  
29 under-sampling mask with signal envelopes along the  $k_y$  and  $t_1$  dimensions is shown on  
30 the left of Figure 5. Select 2D JPRESS spectra from the 4D EP-JRESI data set are shown  
31 in Figure 6 with the spatial distribution of specific spectral peaks in Figure 5.  
32  
33  
34  
35  
36  
37

38 Figure 5 shows the spatial distributions of the Cit peaks highlighted in Figure 6 for the  
39 under-sampled and MaxEnt reconstructed data sets; the purple highlighted voxel  
40 corresponds to the location of the extracted 2D J-resolved spectrum in Figure 6A, the red  
41 corresponds to Figure 6B, and the blue corresponds to Figure 6C. Because of the  
42 sensitivity profile of the endorectal coil, the SNR of voxels close to the rectal wall is  
43 higher than the SNR of voxels further away [42]. The MaxEnt reconstruction in Figure  
44 5B shows the SNR of the Cit peaks in healthy tissue decreasing further from the rectal  
45 wall, as expected. However, the spatial distribution of the under-sampled data set in  
46 Figure 5A shows aliased Cit peaks near the apex of the prostate as well as high SNR  
47 peaks within the rectum that should not be there. The spatial distribution of Cit in the  
48  
49  
50  
51  
52  
53  
54  
55  
56  
57  
58  
59  
60

1  
2  
3 under-sampled data is noisier in general and shows significant spectral-spatial artifacts  
4 when compared to the MaxEnt reconstruction.  
5  
6

7  
8 The top of Figure 6 shows results for the 25% under-sampled 4D EP-JRESI scan and the  
9 bottom shows results for the MaxEnt reconstruction of that scan. Because the scan was  
10 prospectively undersampled, there is no fully sampled data for comparison.  
11  
12

13  
14  
15 Figure 6B shows 2D J-resolved spectra extracted from the 4D NUS EP-JRESI data sets  
16 that are highlighted in red in Figure 5. As shown in the under-sampled spectrum in the  
17 top of the figure, the citrate (Cit) diagonal and its cross peaks around  $F_2=2.6\text{ppm}$  are not  
18 easily resolved. There is significant aliasing of the Cit peaks along  $t_1$  as well as the fat  
19 peaks around  $F_2=1.7\text{ppm}$ . The bottom of the figure shows the same 2D J-resolved  
20 spectrum after MaxEnt reconstruction of the 4D NUS EP-JRESI data set. The Cit  
21 diagonal and cross peaks are now fully resolved with no aliasing along  $t_1$  as well as the  
22 fat peaks around  $F_2=1.7\text{ppm}$ .  
23  
24  
25  
26  
27  
28  
29

30  
31 A high Cit to Cho ratio is normal in healthy prostate tissue, but a low Cit to Cho ratio is  
32 indicative of pathology [43]. Therefore, Figures 6A and 6C show 2D J-resolved spectra  
33 from the 4D EP-JRESI data set from tumors in the left and right base of the prostate that  
34 are highlighted in purple and blue in Figure 5, so they should have decreased Cit and  
35 elevated Cho. The presence of tumors was verified by biopsy with Gleason scores of 3+3  
36 and prostatic specific antigen of 8. The under-sampled spectra in the top of Figure 6C  
37 show Cho peaks at  $F_2=3.2\text{ppm}$  that are highly aliased along  $t_1$  and Figure 6A shows  
38 aliased Cit at  $F_2=2.6\text{ppm}$  from adjacent voxels. The MaxEnt reconstructions are shown in  
39 the bottom of the figure for the same 2D J-resolved spectra. The Cho peaks are no longer  
40 aliased along  $t_1$  and the errant peaks have been removed.  
41  
42  
43  
44  
45  
46  
47  
48

## 49 50 **DISCUSSION**

51  
52 This work addresses the long scan time requirements of 4D MRSI, which is one of the  
53 main issues preventing its widespread adoption. Non-uniform under-sampling was used  
54 to accelerate the 4D data acquisition and MaxEnt non-linear reconstruction was used to  
55  
56  
57  
58  
59  
60

1  
2  
3 rebuild the missing samples. This technique resulted in minimal losses in spatial-spectral  
4 resolution while reducing scan times considerably.  
5  
6

7  
8  
9 The simulated 4D EP-COSY data set results shown in Figure 3 demonstrate how the  
10 MaxEnt reconstruction performs at different levels of noise and percent under-sampling.  
11 The MaxEnt reconstruction decreases the RMSE significantly at each SNR and percent  
12 under-sampling compared to the under-sampled data set but begins to rise at very low  
13 SNR, indicating the inability of MaxEnt to fully reconstruct the data set when features  
14 and sampling artifacts are obscured by high levels of noise. The data fidelity constraint in  
15 equation (3) determines how closely the MaxEnt reconstructed points must be to the  
16 sampled points to within the standard deviation of noise, which increases as the noise  
17 floor increases. This increase in the noise floor effectively “loosens” the fidelity  
18 constraint, which allows the reconstructed points to vary from their sampled counterparts  
19 and increases the entropy of the reconstructed spectrum. As the entropy increases, so too  
20 do the non-linearity and RMSE of the reconstruction with a loose fidelity constraint [44].  
21 The data fidelity constraint can be “tightened” beyond the standard deviation of the noise  
22 in an effort to reduce the RMSE and reconstruction non-linearity but this prevents  
23 MaxEnt from completely removing the spatial-spectral under-sampling artifacts close to  
24 the noise floor, which could potentially obscure small features [27].  
25  
26  
27  
28  
29  
30  
31  
32  
33  
34  
35  
36  
37

38  
39 The results from Figure 3 show the NAA/Cho ratios are consistent with the fully sampled  
40 data set ratios and offer significant improvement over the under-sampled data, even  
41 without using methods to reduce the reconstruction non-linearity [45]; however, the  
42 Lac/Cr ratios deviate slightly from the fully sampled ratios at higher percent under-  
43 sampling and significantly at 20% under-sampling. Upon further investigation, it was  
44 found that each metabolite area used to calculate the NAA/Cho and Lac/Cr ratios, with  
45 the exception of Lac, was stable and consistent with the fully sampled areas over SNR  
46 and percent sampling; however, the areas calculated for Lac were consistently low across  
47 all SNRs for each percent under-sampling. This was caused by a mismatch between the  
48 2D Poisson-gap sample masks that were sine-bell modulated along  $t_1$  and the filtered  
49 signal envelope of Lac, which was thought to be a sine-bell but upon further investigation  
50  
51  
52  
53  
54  
55  
56  
57  
58  
59  
60

1  
2  
3 it was found to be a shifted sine-bell. This shift in the Lac signal envelope meant the  
4 mask failed to sufficiently sample the high SNR Lac points along  $t_1$  for each percent  
5 under-sampling and prevented the full Lac peak area from being reconstructed by  
6 MaxEnt [45] [35] [34]. This discrepancy emphasizes the importance of the sample mask  
7 to the SNR of each reconstructed metabolite for 4D EP-COSI data and the dependence on  
8 the shape of standard filters applied prior to reconstruction [46]. For each metabolite in  
9 EP-JRESI data, however, the maximum SNR point along  $t_1$  is always at  $t_1=1$  and is not  
10 apodized by spectral filters prior to reconstruction; therefore, an exponentially damped  
11 sample mask that only considers  $T_2$  signal losses in the time domain can be used to  
12 sample the high SNR points for each metabolite without the need to consider coherence  
13 transfer signal envelopes.  
14  
15  
16  
17  
18  
19  
20  
21  
22  
23

24 The Poisson-gap sampling masks used in these experiments were generated by a random  
25 Poisson distribution, which injects a degree of uncertainty into the MaxEnt  
26 reconstruction. It has proven to be a robust technique that generates masks with desirable  
27 PSFs, as shown in Figure 2, and the RMSEs of reconstructed data sets using different  
28 Poisson-gap sample masks are stable [32]. Previous attempts by our group to use  
29 deterministic masks that were not randomly generated were difficult to optimize and  
30 suffered from coherent aliasing which cannot be removed by MaxEnt reconstruction [47]  
31 [35]. Recent work in under-sampled multidimensional NMR data sets using deterministic  
32 sample masks has shown promise and could be adapted to 4D MRSI [48]. However,  
33 these sample masks are modulated by an exponential decay function, which is suitable for  
34 EP-JRESI data, but would need to be modified to use a sine-bell function for EP-COSI  
35 data. Poisson-gap sampling has the advantage that it is easily modified to accommodate  
36 different modulation functions and can therefore be used for many different scan types. It  
37 is unknown whether these new deterministic methods are as accommodating as Poisson-  
38 gap in that regard.  
39  
40  
41  
42  
43  
44  
45  
46  
47  
48  
49  
50  
51

52 The healthy human breast results in Figure 4 show that under-sampling and MaxEnt  
53 reconstruction work well for filtered in vivo EP-COSI scans with a sine-bell signal  
54 envelope. The SNR-loss caused by  $T_2$  decay that was not present in the simulated 4D EP-  
55  
56  
57  
58  
59  
60

1  
2  
3 COSI data set did not reduce the efficacy of the reconstruction. There was still sufficient  
4 SNR in the time domain to reconstruct the diagonal and cross peaks in the spectral  
5 domain. The improvement in the ratios of certain lipid peaks shown in Table 2 indicates  
6 the signal from the large diagonal fat peaks that had been aliased over the  $k_y$ - $t_1$  plane by  
7 the under-sampling was returned to the diagonal peaks by MaxEnt reconstruction and  
8 surfaced the smaller UFL and UFR cross peaks that had been obscured. The NUS data set  
9 in Figures 4B1 and 4B2 show artifacts spread along  $t_1$  and  $k_y$  as well as reduced spectral  
10 resolution along  $t_1$  caused by the broad NUS PSF. The homogenous nature of fatty breast  
11 spectra made it difficult to determine from the figure if the spatial resolution along  $k_y$   
12 decreased as a result of the NUS PSF as expected. However, it is clear the effects of the  
13 NUS PSF along  $t_1$  were removed by MaxEnt in Figure 4C1 and the errant spectral peaks  
14 in the spatial distribution were removed in Figure 4C2, suggesting the spatial PSF along  
15  $k_y$  was improved. Any spectral bleed from the spatial PSF of the EP-COSI pulse  
16 sequence along  $k_x$  was orthogonal to the effect of the NUS PSF along  $k_y$  and was not  
17 affected by the MaxEnt reconstruction.  
18  
19  
20  
21  
22  
23  
24  
25  
26  
27  
28  
29  
30

31 Under-sampling of 4D MRSI data can be implemented in the pulse sequence on the  
32 scanner and successfully reconstructed using MaxEnt as shown in Figures 5 and 6 for the  
33 prospectively under-sampled EP-JRESI prostate data. Spatial-spectral artifacts caused by  
34 the broad NUS PSF were removed by MaxEnt to reveal spectra that were spatially  
35 localized in  $k_y$  properly and lacked significant spectral aliasing in  $t_1$ . The Cit multiplet in  
36 the MaxEnt reconstructed data set showed a nicely J-resolved AB-type structure that had  
37 been aliased by convolution with the NUS PSF in the under-sampled data. No  
38 comparisons can be made to the fully sampled data set as was done for the retrospective  
39 EP-COSI data set; however, the mean (Cr+Cho+Spm)/Cit ratio for the MaxEnt  
40 reconstructed 2D JPRESS voxel shown in Figure 6B and the adjacent four voxels within  
41 the prostate, excluding the tumors in the left and right base, is 0.547 with a coefficient of  
42 variation of 21.2% which is consistent with reported literature [43] [49].  
43  
44  
45  
46  
47  
48  
49  
50  
51  
52  
53

54 This work has demonstrated the potential for MaxEnt to accelerate the acquisition of 4D  
55 MRSI data in vivo into clinically acceptable scan times. However, because of its  
56  
57  
58  
59  
60

1  
2  
3 similarity to CS reconstruction, quantitative comparisons between these techniques need  
4 to be made in order to determine the superior method for reconstructing 4D MRSI data  
5 and will be a topic of future research. Additionally, determining whether Poisson-gap or  
6 deterministic sample masks should be used and optimizing the modulation functions for  
7 4D EP-JRESI and EP-COSI data sets and different spectral filters will be addressed in  
8 future papers.  
9

## 10 11 12 13 14 15 **CONCLUSIONS**

16  
17 We have shown that MaxEnt can successfully reconstruct under-sampled 4D MRSI data  
18 by reconstructing a mixed domain spectral-spatial plane. Simulated 4D MRSI data  
19 provided a quantitative characterization of the MaxEnt reconstruction at different percent  
20 under-sampling and SNR and it was shown that in vivo 4D EP-COSI and 4D EP-JRESI  
21 scans could be reconstructed. This acceleration translates into a clinically viable 5 minute  
22 EP-COSI breast scan and 6 minute EP-JRESI prostate scan.  
23  
24  
25  
26  
27  
28

## 29 30 31 **ACKNOWLEDGEMENTS**

32 Authors acknowledge the scientific support of Dr. Rajakumar Nagarajan for recording the  
33 in vivo NUS EP-JRESI data. This work was supported by: 1) a National Institute of  
34 Health (NIH) training grant #5T15 LM07356 (BLB), 2) an IDEA Expansion grant from  
35 the US Army Department of Defense (DOD) Breast Cancer Research Program  
36 (BCRP)#W81XWH-10-1-0743 (MAT), and 3) an IDEA grant from the US Army DOD  
37 Prostate Cancer Research Program (PCRP)#W81XWH-11-1-0248 (MAT).  
38  
39  
40  
41  
42  
43  
44  
45  
46  
47  
48  
49  
50  
51  
52  
53  
54  
55  
56  
57  
58  
59  
60

## References

- 1 Thomas MA, Lipnick S, Velan SS, Liu X, Banakar S, Binesh N, Ramadan S, Ambrosio A, Raylman R, Sayre J, et al. Investigation of breast cancer using two-dimensional MRS. *NMR in Biomed.* 2008;22(1):77-91.
- 2 Kobus T, Vos PC, Hambrock T, De Rooij M, Hulsbergen-Van de Kaa CA, Barentsz JO, Heerschap A, Scheenen TW. Prostate Cancer Aggressiveness: In Vivo Assessment of MR Spectroscopy and Diffusion-weighted Imaging at 3 T. *Radiology.* 2012 Jul 27 DOI: 10.1148/radiol.12111744.
- 3 Kobus T, Hambrock T, Hulsberneg-van de KAA CA. In vivo assessment of prostate cancer aggressiveness using magnetic resonance spectroscopic imaging at 3T with an endorectal coil. *Eur Urol.* 2011;60(5):1074-1080.
- 4 Begley JK, Redpath TW, Bolan PJ, Gilbert FJ. In vivo proton magnetic resonance spectroscopy of breast cancer: a review of the literature. *Breast Cancer Research.* 2012 Apr 19;14(2):207.
- 5 Glunde E, Bhujwalla ZM, Ronen SM. Choline metabolism in malignant transformation. *Nat Rev Cancer.* 2011 Nov 17;11(2):835-848.
- 6 Aue W, Bartholdi E, Ernst R. Two-dimensional spectroscopy. Application to nuclear magnetic resonance. *J. Chem. Phys.* 1976;64:2229-2246.
- 7 Lipnick S, Liu X, Sayre J, Bassett LW, DeBruhl N, Thomas MA. Combined DCE-MRI and single-voxel 2D MRS for differentiation between benign and malignant breast lesions. *NMR in Biomed.* 2010;23(8):922-930.
- 8 Nagarajan R, Gomex A, Raman S, Margolis D, McClure T, Thomas A. Correlation of endorectal 2D JPRESS findings with pathological Gleason scores in prostate cancer patients. *NMR in Biomed.* 2010;23(3):257-261.
- 9 Mansfield P. Spatial mapping of the chemical shift in NMR. *J Phys D Appl Phys.* 1983;16:235-238.
- 10 Mulkern R, Panych L. Echo planar spectroscopic imaging. *Concepts Magn Reson.* 2001;13:213-237.
- 11 Posse S, DeCarli C, Le-Bihan D. 3D echo planar spectroscopic imaging at short echo times in human brain. *Radiology.* 1994;192:733-738.
- 12 Lipnick S, Verma G, Saadallah R, Jon F, Thomas MA. Echo planar correlated spectroscopic imaging: Implementation and pilot evaluation in human calf in vivo. *Magn Reson. Med.* 2010;64(4):947-956.
- 13 Nagarajan R, Furuyama J, Margolis D, Raman S, Sarma M, Thomas MA. Echo planar based J resolved and correlated spectroscopic imaging of human prostate using endorectal coil. In: *ISMRM; 2011; Montreal, Canada.*
- 14 Furuyama JK, Wilson NW, Burns BL, Rajakumar N, Margolis D, Thomas MA. Application of Compressed Sensing to Multidimensional Spectroscopic Imaging in Human Prostate. *Magn. Reson. Med.* 2012;67:1499-1505.
- 15 Donoho D. Compressed Sensing. *IEEE Trans. Info. Theory.* 2006;52(4):1289-1306.
- 16 Candes EJ, Romberg J, Tao T. Robust uncertainty principles: exact signal reconstruction from highly incomplete frequency information. *IEEE Trans. Info.*

- 1  
2  
3  
4 Theory. 2006;52(2):489-509.
- 5 17 Lustig M, Donoho D, Pauly JM. Sparse MRI: The application of compressed sensing  
6 for rapid MR imaging. *Magn. Reson. Med.* 2007;53(6):1182-1195.
- 7  
8 18 Block KT, Uecker M, Frahm J. Undersampled radial MRI with multiple coils.  
9 Iterative image reconstruction using a total variation constraint. *Magn. Reson. Med.*  
10 2007;57(6):1086-1098.
- 11 19 Hu S, Lustig M, Chen A, Crane J, Kerr A, Kellet D, Hurd R, Kurhanewicz J, Nelson  
12 S, Pauly J, et al. Compressed Sensing for Resolution Enhancement of Hyperpolarized  
13 C13 Flyback 3D-MRSI. *J. Magn. Reson.* 2008;192:258-264.
- 14  
15 20 Gamper U, Boesiger P, Kozerke S. Compressed sensing in dynamic MRI. *Magn*  
16 *Reson Med.* 2008;59:365-373.
- 17  
18 21 Jung H, Kyunghyun S, Nayak KS, Kim E, Ye JC. k-t FOCUSS: A general compressed  
19 sensing framework for high resolution dynamic MRI. *Magn Reson Med.*  
20 2009;61(1):103-116.
- 21  
22 22 Provost J, Lesage F. The Application of Compressed Sensing for Photo-Acoustic  
23 Tomography. *IEEE Trans Med Imag.* 2009;28(4):585-594.
- 24  
25 23 Herman M, Strohmer T. Compressed sensing radar. In: 2008 IEEE Radar Conference  
26 (RADAR); 2008; Rome, Italy.
- 27  
28 24 Frieden RB. Restoring with Maximum Likelihood and Maximum Entropy. *J. Optical.*  
29 *Soc. Am.* 1972;62(4):511-518.
- 30  
31 25 Skilling J, Bryan RK. Maximum Entropy Image Reconstruction: General Algorithm.  
32 *Mon. Not. R. Astr. Soc.* 1984;211(1):111-124.
- 33  
34 26 Daniell GJ, Hore PJ. Maximum Entropy and NMR-A New Approach. *J. Magn. Reson.*  
35 1989;4(3):515-536.
- 36  
37 27 Hoch J, Stern AS. *NMR Data Processing.* New York, NY: Wiley; 1996.
- 38  
39 28 Shannon CE. A Mathematical Theory of Communication. *Bell Sys. Tech. Journal.*  
40 1948;27:379-423, 623-656.
- 41  
42 29 Smith SA, Levante TO, Meier BH, Ernst RR. Computer Simulations in Magnetic  
43 Resonance. An Object-Oriented Programming Approach. *JMR.* 1994;106(1):75-105.
- 44  
45 30 Thomas MA, Yue K, Binesh N, Davanzo P, Kumar A, Siegel B, Frye M, Curran J,  
46 Lufkin R, Martin P, et al. Localized two-dimensional shift correlated MR  
47 spectroscopy of human brain. *MRM.* 2001;46(1):58-67.
- 48  
49 31 Pierpaoli C, Basser PJ. Toward a Quantitative Assessment of Diffusion Anisotropy.  
50 *MRM.* 1996;36:893-906.
- 51  
52 32 Hyberts SG, Takeuchi K, Wagner G. Poisson-Gap Sampling and Forward Maximum  
53 Entropy Reconstruction for Enhancing the Resolution and Sensitivity of Protein NMR.  
54 *J. Am. Chem. Soc.* 2010;132:2145-2147.
- 55  
56 33 Maciejewski MW, Mobli M, Schuyler A, Stern A, Hoch J. Data Sampling in  
57 Multidimensional NMR: Fundamentals and Strategies. *Top. Curr. Chem.*  
58 2011;316:49-77.
- 59  
60 34 Mobli M, Hoch JC. Maximum Entropy Spectral Reconstruction of Nonuniformly  
Sampled Data. *CMR.* 2008;32A(6):436-448.

- 1  
2  
3  
4 35 Schmieder P, Stern A, Wagner G, Hoch J. Applications of Nonlinear Sampling  
5 Schemes to COSY-type spectra. *J. Biomolecular NMR*. 1993;3(5):569-576.
- 6 36 Marseille GJ, De Beer R, Fuderer M, Mehlkopf AF, van Ormondt D. Nonuniform  
7 Phase-encode Distributions for MRI Scan Time Reduction. *J. Magn. Reson. Series B*.  
8 1996;111:70-75.
- 9 37 Devroye L. *Non-Uniform Random Variate Generation*. New York, NY: Springer-  
10 Verlag; 1986.
- 11 38 Dippe M, Wold E. Antialiasing Through Stochastic Sampling. *ACM SIGGRAPH*  
12 *Computer Graphics*. 1985;19(3):69-78.
- 13 39 Cook R. Stochastic Sampling in Computer Graphics. *ACM Trans. Comp. Graphics*.  
14 1986;5(1):51-72.
- 15 40 Frieden R. Unified Theory for Estimating Frequency-of-Occurrence Laws and Optical  
16 Objects. *J. Opt. Soc. Am*. 1983;73(7):927-938.
- 17 41 Constable RT, Henkelmen RM. Why MEM Does Not Work in MR Image  
18 Reconstuction. *Magn. Reson. Med*. 1990;14:12-25.
- 19 42 Outwater EK, Petersen RO, Siegelman ES, Gomella LG, Chernesky CE, Mitchell DG.  
20 Prostate carcinoma: assessment of diagnostic criteria for capsular penetration on  
21 endorectal coil MR images. *Radiology*. 1994;193:333-339.
- 22 43 Wang X, Wang B, Gao Z, Liu Z, Sun Q, Yuan Y. 1H-MRSI of prostate cancer: the  
23 relationship between metabolite ratio and tumor proliferation. *Eur J Radiol*.  
24 2010;73:345-351.
- 25 44 Hoch J, Stern A, Donoho D, Johnstone IM. Maximum Entropy Reconstruction of  
26 Complex (Phase-Sensitive) Spectra. *J. Magn. Reson*. 1990;86:236-246.
- 27 45 Schmeider P, Stern A, Wagner G, Hoch J. Quantification of Maximum-Entropy  
28 Spectrum Reconstructions. *J Magn. Reson*. 1997;125:332-339.
- 29 46 Ziegler A, Izquierdo M, Decorps M. Optimization of Homonuclear Two-Dimensional  
30 Correlation Methods for in vivo and ex vivo NMR. *J. Magn. Reson. Series B*.  
31 1995;107:10-18.
- 32 47 Barna J, Laue E, Mayger M, Skilling J, Worrall S. Exponential Sampling, an  
33 Aternative Method for Sampling in Two-Dimensional NMR Experiments. *J. Magn.*  
34 *Reson*. 1987;73:69-77.
- 35 48 Eddy M, Ruben D, Griffin R, Herzfeld J. Deterministic schedules for robust and  
36 reproducible non-uniform sampling in multidimensional NMR. *J. Magn. Reson*.  
37 2012;214:296-301.
- 38 49 Mueller-Lisse U, Scherr M. Proton MR spectroscopy of the prostate. *Eur J Radiol*.  
39 2007;63:351-360.
- 40 50 Aue W, Bartholdi E, Ernst E. Two-dimensional spectroscopy. Application to nuclear  
41 magnetic resonance. *J. Chem. Phys*. 1976;64:2229-2246.
- 42 51 Boyd S, Vandenberghe L. *Convex Optimization*. Cambridge: Cambridge University  
43 Press; 2004.
- 44 52 Candes E, Wakin M, Boyd S. Enhancing Sparsity by Reweighted l1 Minimization. *J.*  
45 *Fourier. Anal. Appl*. 2008;14:877-905.
- 46  
47  
48  
49  
50  
51  
52  
53  
54  
55  
56  
57  
58  
59  
60

- 1  
2  
3  
4 53 Jaynes ET. Information Theory and Statistical Mechanics. Phys. Review.  
5 1957;106(4):620-630.  
6  
7 54 Silverman H, Shapiro R. Alias Free Sampling of Random Noise. SIAM.  
8 1960;8(2):225-248.  
9  
10 55 Stern A, Donoho D, Hoch J. NMR data processing using iterative thresholding and  
11 minimum l1-norm reconstruction. J. Magn. Reson. 2007;188:295-300.  
12  
13 56 Tropp J, Gilbert A. Signal Recovery From Partial Information via Orthogonal  
14 Matching Pursuit. IEEE Trans. Info. Theory. 2007;53:4655-4666.  
15  
16  
17  
18  
19  
20  
21  
22  
23  
24  
25  
26  
27  
28  
29  
30  
31  
32  
33  
34  
35  
36  
37  
38  
39  
40  
41  
42  
43  
44  
45  
46  
47  
48  
49  
50  
51  
52  
53  
54  
55  
56  
57  
58  
59  
60

**Table 1: PPM locations for metabolite peaks used in ratio calculations**

	<i>NAA</i>	<i>Cho</i>	<i>Cr</i>	<i>Lac</i>
Diagonals (ppm)	(2.0,2.0), (2.5,2.5), (4.3, 4.3)	(3.2,3.2), (3.5,3.5), (4.0,4.0)	(3.1,3.1), (3.9,3.9)	(1.3,1.3), (4.1,4.1)
Cross Peaks (ppm)	(2.5,4.3), (4.3,2.5)	(3.5,4.0), (4.0,3.5)	N/A	(1.3,4.1), (4.1,1.3)

**Table 2: Range and mean error of (UFL+UFR)/(FAT3+FAT2) integrated peak area ratios for fully sampled, NUS, and MaxEnt reconstruction.**

	Ratio Range	Mean Ratio Error
Full	0.1840 - 0.0634	N/A
MaxEnt	0.1604 - 0.0550	0.0188 ± .0048
NUS	0.4262 - 0.2180	0.1737 ± .0459

## FIGURE LEGENDS

**Figure 1:** Simulated quad phantom illustration. (Top) Spatial distribution of an NAA, Cr, Cho, and Lac diagonal peak when fully sampled. (Bottom) Spatial distribution of the same NAA, Cr, Cho, and Lac diagonal peak as above with 25% under-sampling in the  $k_y$ - $t_1$  plane.

**Figure 2:** Poisson sample mask creation along the  $k_y$ - $t_1$  plane for EP-JRESI and EP-COSI. (Top) Sine and exponentially modulated values for  $\lambda$ . (Upper Middle) Poisson distributed values for each  $\lambda$  indicating the sample gap between that point and other points in the sample distribution. (Lower Middle) Resulting 2D Poisson-gapped sample mask. (Bottom) Magnitude PSF of the 2D sample mask.

**Figure 3:** Metrics comparing the under-sampled, MaxEnt reconstruction, and fully sampled 4D EP-COSI simulated data. (Left) RMSE of under-sampled and MaxEnt reconstructed data versus SNR for 20, 40, 60, and 80% under-sampling. (Right) Comparison of the NAA/Cho and Cr/Lac ratios for fully sampled data to MaxEnt (Top) and under-sampled (bottom) reconstruction versus SNR for 20, 40, 60, and 80% under-sampling

**Figure 4:** (Left) Under-sampling mask used to retrospectively under-sample the  $k_y$ - $t_1$  plane to 25% (Top) Selected 2D COSY spectrum from a 4D EP-COSI scan of healthy, fatty breast highlighted in the bottom images for A1) fully sampled B1) 25% under-sampling C1) MaxEnt reconstruction (Bottom) Spatial distribution of the olefinic cross-peaks of unsaturated fatty acids (UFL/UFR) highlighted in the 2D COSY spectrum for A2) fully sampled B2) 25% under-sampling C2) MaxEnt reconstruction.

**Figure 5:** Spatial distribution of the citrate peaks from a 4D EP-JRESI scan of malignant prostate highlighted in the 2D JPRESS spectra from Figure 6 for (A) 25% Under-sampled (B) MaxEnt reconstructed. (Left) Mask used to prospectively under-sample the  $k_y$ - $t_1$  plane to 25%.

**Figure 6:** Select 2D J-resolved spectra from a 4D EP-JRESI scan of malignant prostate for (top) prospectively 25% under-sampled and (bottom) MaxEnt reconstructed. A) Spectra highlighted in purple in Figure 5 showing elevated Choline and depressed Citrate in a malignant lesion. B) Spectra highlighted in red in Figure 5 showing elevated Citrate and normal Choline in healthy prostate. C) Spectra highlighted in blue in Figure 5 showing elevated Choline and depressed Citrate in a malignant lesion.

1  
2  
3  
4  
5  
6  
7  
8  
9  
10  
11  
12  
13  
14  
15  
16  
17  
18  
19  
20  
21  
22  
23  
24  
25  
26  
27  
28  
29  
30  
31  
32  
33  
34  
35  
36  
37  
38  
39  
40  
41  
42  
43  
44  
45  
46  
47  
48  
49  
50  
51  
52  
53  
54  
55  
56  
57  
58  
59  
60

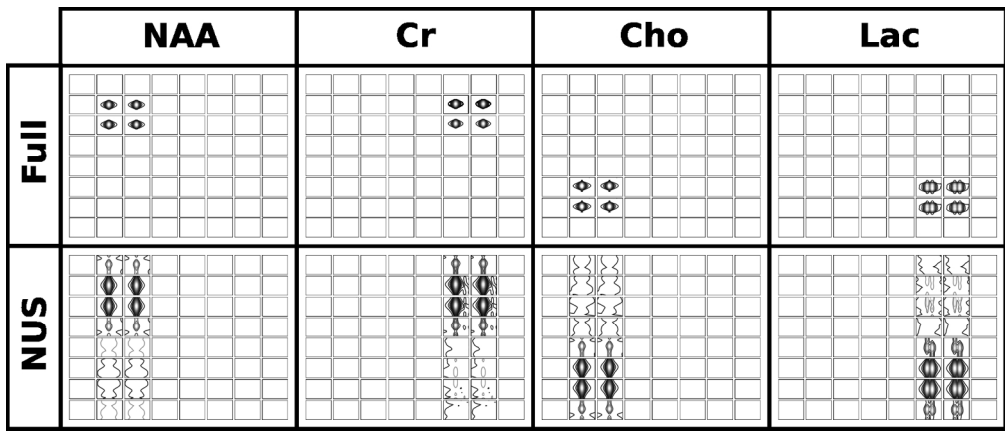


Figure 1: Simulated quad phantom illustration. (Top) Spatial distribution of an NAA, Cr, Cho, and Lac diagonal peak when fully sampled. (Bottom) Spatial distribution of the same NAA, Cr, Cho, and Lac diagonal peak as above with 25% under-sampling in the ky-t1 plane.

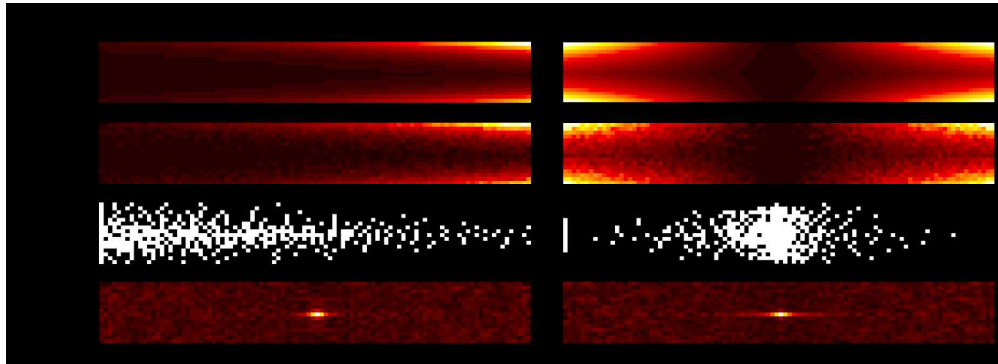


Figure 2: Poisson sample mask creation along the  $ky$ - $t_1$  plane for EP-JRESI and EP-COSI. (Top) Sine and exponentially modulated values for  $\lambda$ . (Upper Middle) Poisson distributed values for each  $\lambda$  indicating the sample gap between that point and other points in the sample distribution. (Lower Middle) Resulting 2D Poisson-gapped sample mask. (Bottom) Magnitude PSF of the 2D sample mask.

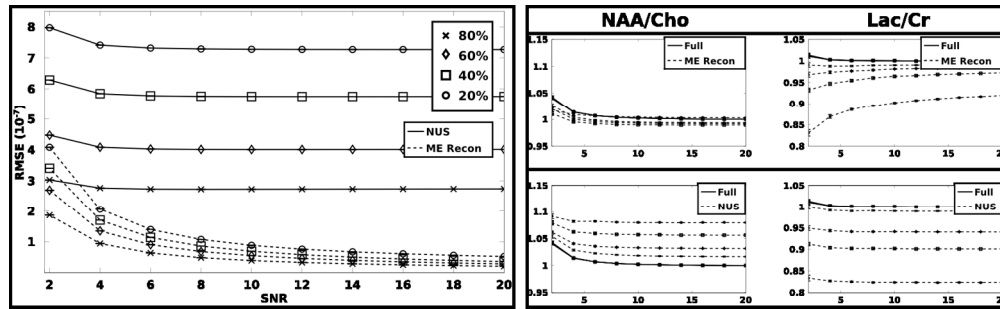


Figure 3: Metrics comparing the under-sampled, MaxEnt reconstruction, and fully sampled 4D EP-COSY simulated data. (Left) RMSE of under-sampled and MaxEnt reconstructed data versus SNR for 20, 40, 60, and 80% under-sampling. (Right) Comparison of the NAA/Cho and Cr/Lac ratios for fully sampled data to MaxEnt (Top) and under-sampled (bottom) reconstruction versus SNR for 20, 40, 60, and 80% under-sampling

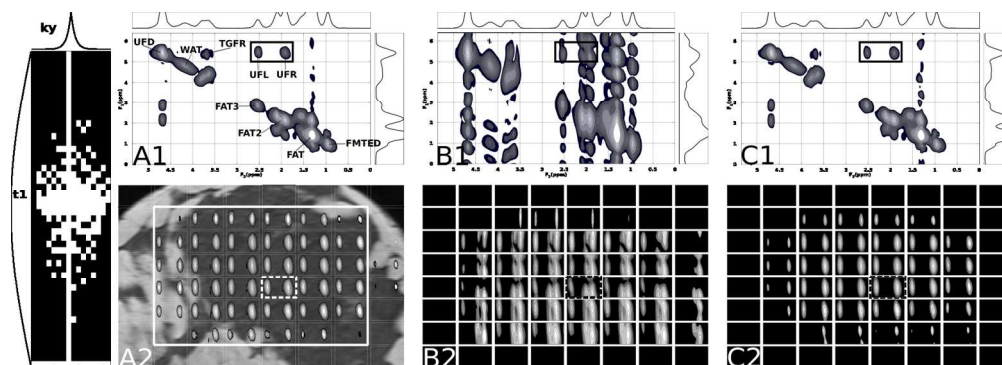


Figure 4: (Left) Under-sampling mask used to retrospectively under-sample the  $ky$ - $t_1$  plane to 25% (Top) Selected 2D COSY spectrum from a 4D EP-COSI scan of healthy, fatty breast highlighted in the bottom images for A1) fully sampled B1) 25% under-sampling C1) MaxEnt reconstruction (Bottom) Spatial distribution of the olefinic cross-peaks of unsaturated fatty acids (UFL/UFR) highlighted in the 2D COSY spectrum for A2) fully sampled B2) 25% under-sampling C2) MaxEnt reconstruction.

1  
2  
3  
4  
5  
6  
7  
8  
9  
10  
11  
12  
13  
14  
15  
16  
17  
18  
19  
20  
21  
22  
23  
24  
25  
26  
27  
28  
29  
30  
31  
32  
33  
34  
35  
36  
37  
38  
39  
40  
41  
42  
43  
44  
45  
46  
47  
48  
49  
50  
51  
52  
53  
54  
55  
56  
57  
58  
59  
60

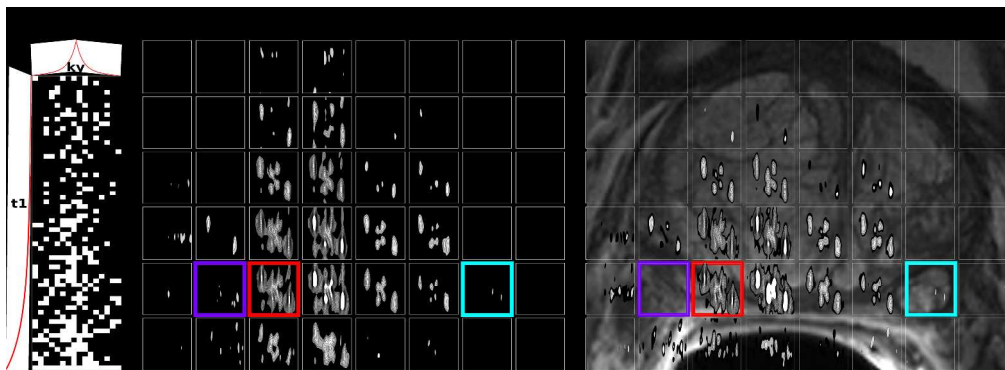


Figure 5: Spatial distribution of the citrate peaks from a 4D EP-JRESI scan of malignant prostate highlighted in the 2D JPRESS spectra from Figure 6 for (A) 25% Under-sampled (B) MaxEnt reconstructed. (Left) Mask used to prospectively under-sample the ky-t1 plane to 25%.

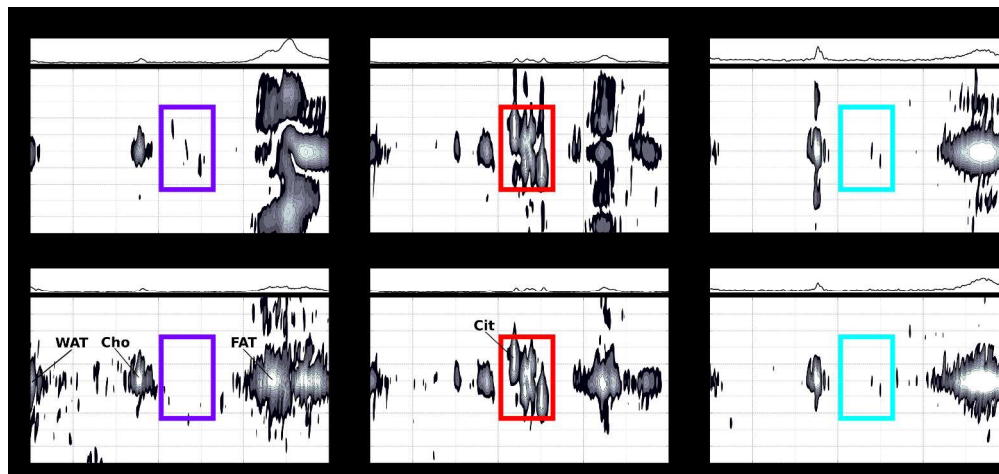


Figure 6: Select 2D J-resolved spectra from a 4D EP-JRESI scan of malignant prostate for (top) prospectively 25% under-sampled and (bottom) MaxEnt reconstructed. A) Spectra highlighted in purple in Figure 5 showing elevated Choline and depressed Citrate in a malignant lesion. B) Spectra highlighted in red in Figure 5 showing elevated Citrate and normal Choline in healthy prostate. C) Spectra highlighted in blue in Figure 5 showing elevated Choline and depressed Citrate in a malignant lesion.